

---

# Interaction of multiple micro-defects on the strength and failure mechanism of UD composites by computational micromechanics

Chenyang Xie<sup>1</sup>, Lishuai Sun<sup>1</sup>, Junzhen Chen<sup>1</sup>, Zhiyong Zhao<sup>2</sup>, Junbiao Wang<sup>1</sup>, Jianjun Jiang<sup>1</sup>,  
Yujun Li<sup>1, \*</sup>

*1 School of Mechanical Engineering, Northwestern Polytechnical University, Xi'an 710072, China*

*2 Wuhan Second Ship Design and Research Institute, Wuhan 430205, PR China*

*\*Corresponding author. Email: li.yujun@nwpu.edu.cn (Y. Li)*

**Abstract:** The mechanical properties of unidirectional fiber-reinforced plastic (UD-FRP) are affected by a variety of micro-defects, such as random fiber arrangement, fiber misalignment and micro-voids. This study aims to investigate how these multiple micro-defects interact with each other and how they affect the strength and failure mechanisms of UD-FRP by means of computational micromechanics. The composite behavior was simulated by the finite element analysis of a representative volume element of the composite microstructure in which the random distribution of fibers, the micro-voids, and the fiber misalignment are explicitly included. Both matrix and interface failure were considered for the loadings of transverse tension/compression, longitudinal compression, transverse/ longitudinal shear, and their combination. It was found that these three micro-defects significantly weakened the compressive strength of UD-FRP along the longitudinal direction. Especially, the fiber misalignment magnified the effect of fiber arrangement, while the micro-voids reduce the effect. Besides, the fiber arrangement and micro-voids significantly weakened the tensile and compressive strength of UD-FRP along the transverse direction, but their interaction effect was not obvious. Moreover, transverse and longitudinal shear strength are significantly affected by micro-voids, but only longitudinal shear is affected by geometric fiber arrangement, and this effect is also weakened by micro-voids. Finally, the damage envelope under the combined longitudinal compression and transverse loads was obtained and compared with the Tsai-Wu failure criterion. The results showed that the Tsai-Wu criteria can provide an effective estimation for the failure locus under this biaxial loading condition.

**Keywords:** Polymer-matrix composites; Computational mechanics; Strength; Geometrical fiber arrangement; Fiber misalignment; Micro-voids.

## 1. Introduction

Due to the superior mechanical qualities, fiber-reinforced plastic (FRP) composites are increasingly utilized in the construction, energy, aviation, and marine industries. A unidirectional fiber-reinforced plastic (UD-FRP) ply is the most basic element of a composite material. Most UD-FRPs have a certain level of microstructural defects, which could lead to uncertainty in the mechanical behavior [1-3]. One example is the failure response, which has significant variation compared to the theoretical prediction [4-7]. The difference is primarily caused by the microscopic configuration characteristics, such as the various fiber, matrix, and interface defects [8, 9]. These defects occur during the manufacturing process in the form of variations in the spatial fiber arrangement, matrix micro-voids, and imperfect interface. The role of such defects needs special attention, but effectively capturing their effects on the degradation of mechanical properties remains a major challenge.

The investigations on the influence of common microscopic defects in UD-FRP are summarized and listed in Table 1. Research on the geometric fiber arrangement focuses mainly on its impact on the transverse failure response, while research on fiber misalignment (also called fiber waviness) focuses mainly on the longitudinal compressive properties. The influence of micro-voids on various

mechanical behavior has been widely investigated. Fiber breakage and imperfect interface are also microscopic defects of UD-FRP, but with the development of manufacturing technology, fiber breakage, and imperfect interface are no longer particularly common defects. This study is limited to geometrical fiber arrangement, fiber misalignment, and micro-voids, which are considered the most significant types of defects in UD-FRP.

Table 1. Summary of investigations on the influence of common microscopic defects in UD-FRP

Mechanical properties Defect type	Transverse tension	Transverse compression	Transverse shear	Longitudinal tension	Longitudinal compression	Longitudinal shear
Fiber arrangement	[10-14]	[12, 13]	[10, 14, 15]	\	\	\
Fiber misalignment	[16]	[16]	[17]	[16, 18]	[16-19]	[17]
Matrix micro-voids	[16, 20-24]	[16, 20-23]	[20-23]	[16, 23]	[16, 23-25]	[20, 22, 23]

Most of the previous modeling efforts on the fiber arrangement rely on idealizing the composite microstructure without realistically incorporating the geometric features. The actual fibers are arranged in a random way, as shown in Figure 1(a). The small inter-fiber distance caused by the random arrangement of fibers would cause a high local stress concentration, which is the main cause of local interface damage and thus lead to earlier damage of the matrix [10, 15]. Consequently, the randomness of fiber arrangement has a strong influence on the damage initiation dominated by FRP interfaces [11]. Under tension/compression loading in the transverse direction, the more irregular the fiber distribution is, the earlier the damage to UD-FRP initiates. Compared with the ideal fiber arrangement, both transverse tensile and compressive strengths of UD-FRP with randomly distributed fibers have a certain tendency to decrease [12]. In addition, resin-rich zones, as a typical micro defect caused by fiber arrangement, would result in large uncertainty in the transverse mechanical properties, but their effect on the transverse strength has no significant weakening trend [13].

Furthermore, the manufacturing process of FRP could cause small-angle fiber misalignment in each ply [26-28]. Misaligned fibers deteriorate the compressive strength of UD-FRP, in particular by introducing localized micro-buckling under longitudinal compressive loading [29, 30]. At a fiber misalignment angle of  $5^\circ$ , the compressive strength of the laminate can drop to 84% of its original strength [16]. Therefore, the fiber misalignment level plays a key role, and a number of techniques have been developed to characterize fiber orientations, such as image analysis of 2D optical microscopy [31] and X-ray computed tomography [32]. The measured data can then be integrated with analytical or numerical methods for the quality analysis of composite laminates [19, 28]. The fiber misalignment in actual FRP, however, is non-uniform, as depicted in Figure 1(b). Recently, Catalanotti et al. developed a semi-random algorithm to characterize fiber misalignment in a statistical way [32, 33]. The fiber was divided into a series of connected spheres, and a random perturbation process was then applied to these spheres to achieve the specified fiber misalignment. Fiber misalignment was found to significantly weaken the compressive strength of UD-FRP in the longitudinal direction but to have little effect on strength, damage initiation, and damage propagation in shear directions (including longitudinal and transverse shear) [17, 18]. It is worth noting that the random perturbation process works in a geometric manner, ignoring the deformation consistency of the fibers. It may lead to excessive local distortion of the fibers, even if the generated fiber architecture agrees well with the measured values in the statistical sense. Therefore, it is necessary to consider both the geometric and physical properties of the fibers when creating

representative volume element (RVE) models that resemble realistic microstructures.

Another significant type of defect in FRP is matrix voids, which can significantly degrade the matrix- and interface-dominated mechanical properties. The matrix voids include two typical types, namely meso-voids, and micro-voids. Meso-voids appear in the resin-rich areas between tows and are generally spherical, while micro-voids are formed between the fibers in tow in the form of long ellipsoids or cylindrical shapes [34], as shown in Figure 1(c). It is difficult to control the micro-voids content, which significantly affects the mechanical properties of UD-FRP. Aiming at micro-voids' influence on FRP's transverse mechanical properties, Hyde et al. developed a finite element framework based on computational microscopic mechanics to establish a two-dimensional RVE model of UD-FRP containing micro-voids so as to investigate the influence of micro-voids on the mechanical properties of UD-FRP [20]. The results show that the micro-voids have a significant impact on the loading mode dominated by matrix damage. Because of the stress concentration close to the micro-voids, the matrix is more susceptible to plastic deformation and damage behavior, reducing strength. As the loading increases, damage propagates from the void to the whole RVE, leading to global failure and material softening and ultimately resulting in significantly reduced transverse strength of UD-FRP [20, 21]. Thus, the micro-voids reduce the modulus and strength in tension, compression and shear along the transverse direction, as well as the modulus and strength in compression along the longitudinal direction. Particularly, the fibers in the local area near the voids are more likely to form the fiber kink-band under longitudinal compression [25]. On the other hand, the micro-voids have little influence on the longitudinal tension since the longitudinal load is mainly supported by fibers [23]. However, quantitative studies on the influence of micro-voids on CFRP composites under various loading conditions are still lacking, as mentioned by He et al [22].

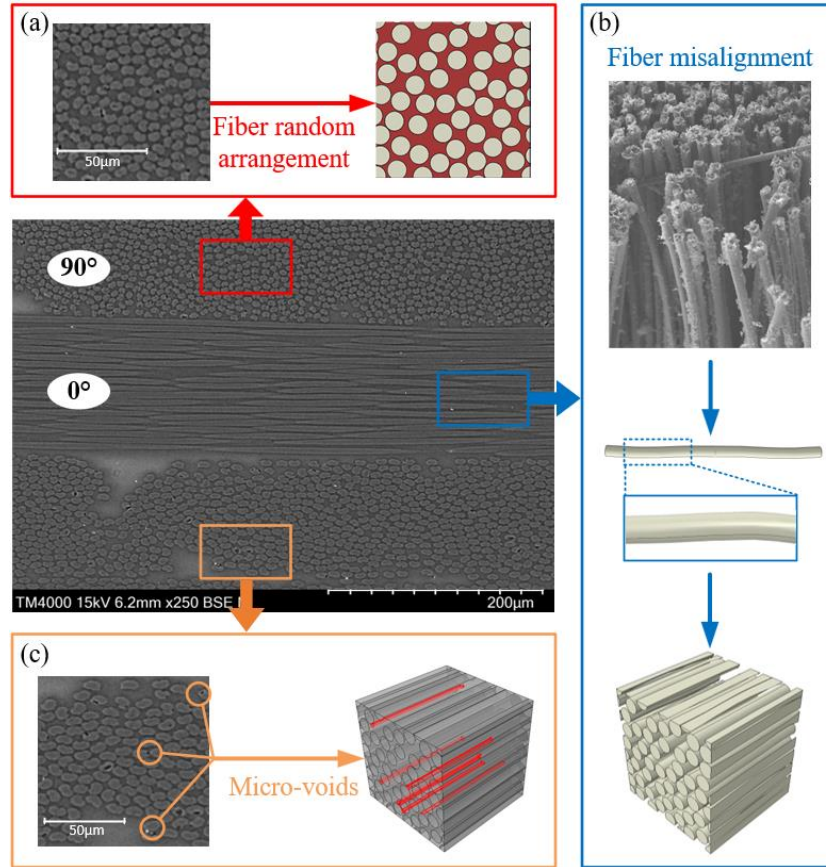


Fig. 1. Micro-defects in UD-FRP: (a) geometrical fiber arrangement, (b) fiber misalignment, and (c) micro-voids in the matrix.

The effects of geometrical fiber arrangement, fiber misalignment, and micro-voids on various mechanical properties of UD-FRP have been thoroughly discussed in previous work. It has shown that these defects have little effect on the properties of longitudinal tension but have a great effect on the properties of longitudinal compression, transverse tension/compression, longitudinal shear and transverse shear. However, the vast majority are limited to analyzing a single defect's influence on the mechanical response, while their interaction has not yet been evaluated. This interaction is, however, important as these defects interact with each other at the microscale and thus have global influence at higher scales. If we have a better understanding of how controllable defects affect strength, we can hope to design stronger composites, depending on their applications. In this study, a realistic representation of the microstructure of UD-FRP was created to consider the spatial distribution of fibers and matrix voids explicitly, and then a micromechanical computational model was developed to predict the failure behavior. The effects of fiber arrangement, misalignment, and void content on the overall stress-strain behavior of UD-FRP were analyzed. These analysis made it possible to determine the failure locus of UD-FRP when loaded in longitudinal compression, transverse tension/compression and longitudinal/transverse shear.

## 2. Computational framework

The general procedure for generating the RVE is given to introduce three common microscopic defects, i.e., fiber arrangement, fiber misalignment, and micro-voids. Then the appropriate constitutive models are presented for the fiber, matrix, and fiber-matrix interface. A coupled plasticity-damage model and a cohesive zone model are adopted, assuming that damage will be developed only in the matrix and at the fiber-matrix interface.

### 2.1. Generation of the RVE

To generate 3D-RVE, 2D-RVE of the UD-FRP cross section is constructed considering different geometrical fiber arrangements. It is then utilized to create 3D-RVEs that satisfy the required fiber volume fraction, diameter, and boundary length under the ideal and random fiber arrangement. Fiber misalignment is a microscopic defect on fibers, while micro-voids only exist in the matrix. Therefore, the 3D geometric models of the fibers and the matrix, each containing its own specific defects, are generated based on the previously created 2D-RVE. Finally, the RVE containing geometric fiber arrangement, fiber misalignment, and micro-voids are integrated together through Boolean operations.

#### 2.1.1. Geometrical fiber arrangement

2D-RVE can represent the geometrical fiber arrangement by considering the position of each fiber. The critical point is to determine each circular fiber's center coordinates. Many methods have been proposed to generate 2D-RVE with a given fiber volume fraction and distribution. This paper adopts the random perturbation method proposed by Wongsto and Li [14] (later extended by Catalanotti [35]), which is a simplified version of the discrete element method (DEM) based approach. This method involves three steps: filling, expansion, and perturbation, as shown in Figure 2(a-b). Using the fiber volume fraction  $v_f$ , fiber radius  $d_f$ , and dimensions of the 2D-RVE  $L$  as initial inputs, a compact configuration with hexagonal fiber packing can be obtained for the calculated number of fibers. Then, the compact RVE is expanded to the desired fiber volume fraction by scaling the center coordinates of each fiber, yielding the RVE with the ideal fiber arrangement. Finally, a perturbation process that moves the fibers randomly results in the final RVE, as shown in Figure 2(c). The 2D-RVE generated by this procedure has a specified volume fraction  $v_f = 58.9\%$ , fiber diameter  $d_f = 9 \mu\text{m}$ , and the 2D-RVE cross-sectional size  $L = 72 \mu\text{m}$  (see Section 2.3 for cross-sectional size determination), which prevents neighboring fibers from entering one another and guarantees geometric periodicity.

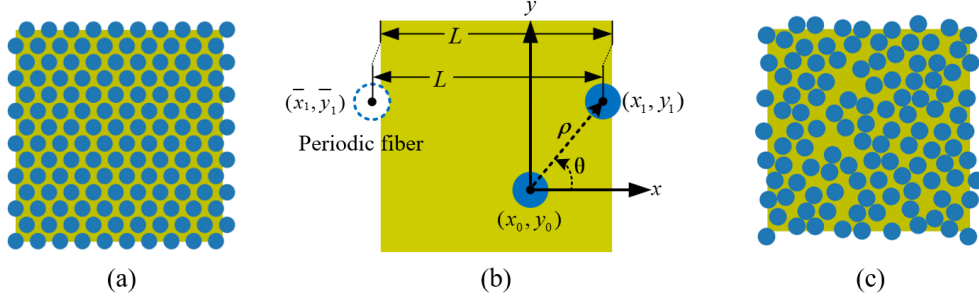


Fig. 2. The process to generate random fiber arrangement: (a) expansion, (b) perturbation, and (c) final 2D-RVE

### 2.1.2. Fiber misalignment

In order to appropriately represent the fiber misalignment, each fiber is characterized as a Bézier curve determined by  $n_c$  control points. As shown in Figure 3, these control points are generated by a random walk process, created one by one starting from the points in the 2D-RVE. The value of  $n_c$  depends on the longitudinal length  $H$  of RVE as  $n_c = H/d_f$ . The coordinates of each control point are controlled by the multivariable von-Mises Fischer distribution, and different fiber misalignment levels are achieved by changing the reliability parameters of the distribution. The distribution is given as:

$$f(\mathbf{u}_2^{(i)} | \boldsymbol{\mu}_1, k_1, \boldsymbol{\mu}_2^{(i-1)}, k_2) = \frac{|k_1 \boldsymbol{\mu}_1 + k_2 \boldsymbol{\mu}_2^{(i-1)}|}{2\pi \left( e^{|k_1 \boldsymbol{\mu}_1 + k_2 \boldsymbol{\mu}_2^{(i-1)}|} - e^{-|k_1 \boldsymbol{\mu}_1 + k_2 \boldsymbol{\mu}_2^{(i-1)}|} \right)} \cdot e^{k_1 \boldsymbol{\mu}_1^T \mathbf{u}_2^{(i)} + k_2 \boldsymbol{\mu}_2^{(i-1)T} \mathbf{u}_2^{(i)}} \quad (1)$$

where  $\boldsymbol{\mu}_2^{(i)}$  represents the target direction at the  $i_{th}$  control point. It is controlled by the principal direction  $\boldsymbol{\mu}_1$  of UD-RVE and the direction  $\boldsymbol{\mu}_2^{(i-1)}$  at the previous control point.  $k_1$  and  $k_2$  are the reliability parameters used to control the corresponding correlation. The greater the reliability parameter, the stronger the correlation. Based on the above process, the misaligned fibers have been characterized as Bezier curves one by one, the implementation details of the random walk process can be found in [36].

The orientation of the fibers created based on the random walk algorithm in the above research is randomly distributed in space, and complex adjustment procedures are required to achieve consistency in the main direction of each fiber and the geometric periodicity of RVE. This study optimized the method to quickly generate RVE for UD-FRP, mainly involving the overall rotation of each fiber and the application of periodic conditions. In order to facilitate the implementation of the following steps, the Bézier curve of each fiber is dispersed into a sphere chain with equal distance, and the number of fiber spheres on the sphere chain  $n_s$  is not strictly limited so as to ensure the smoothness of the fiber. For the  $j_{th}$  fiber,  $\mathbf{e}$  is the normal vector of the average direction of each fiber before the fiber rotation  $\boldsymbol{\mu}_1^j$  and the principal direction  $\boldsymbol{\mu}_1$ ,  $\alpha$  is the deflection angle of  $\boldsymbol{\mu}_1^j$  relative to  $\boldsymbol{\mu}_1$ , and  $\boldsymbol{\omega}$  is the direction of the  $k_{th}$  ( $k=1, \dots, n_s$ ) sphere  $s^k$  relative to the first sphere  $s^1$  before rotation, which is determined by the coordinates of the  $k_{th}$  sphere  $x_i^k$  and the first sphere  $x_i^1$ :

$$\boldsymbol{\omega} = x_i^k - x_i^1 (i = 1, 2, 3) \quad (2)$$

$$\mathbf{e} = \boldsymbol{\mu}_1 \times \boldsymbol{\mu}_1^j \quad (3)$$

Then the rotation matrix  $\mathbf{D}_i$  is defined as:

$$\mathbf{D}_i(\boldsymbol{\omega}, \mathbf{e}, \alpha) = (\mathbf{e} \cdot \boldsymbol{\omega})\mathbf{e} + ((\mathbf{e} \times \boldsymbol{\omega}) \times \mathbf{e}) \cos \alpha + (\mathbf{e} \times \boldsymbol{\omega}) \sin \alpha \quad (4)$$

where " $\cdot$ " represents the scalar product and " $\times$ " represents the cross product. Therefore, the coordinates of the center point of the  $k_{th}$  sphere on the fiber after rotation  $\bar{x}_i^k$  can be expressed as the sum of the coordinates of the rotation matrix  $\mathbf{D}_i$  and the first sphere on the fiber:

$$\bar{x}_i^k = x_i^1 + \mathbf{D}_i(\boldsymbol{\omega}, \mathbf{e}, \alpha) (i=1, 2, 3) \quad (5)$$

By rotating each fiber, the average orientation of each fiber curve is consistent with the longitudinal direction of RVE. Meanwhile, in order to ensure the periodicity of the RVE, the rotation matrix has been used to ensure the geometric periodicity of RVE along the axial direction (Z-direction). In order to achieve periodicity in the other two directions (X- and Y-directions), in-plane periodicity conditions are separately set for the fiber spheres at boundary on each plane  $P^k$  ( $k=1, \dots, n_s$ ):

$$\lambda_i^k (i=1, 2) = \begin{cases} L, \bar{x}_i^k \leq r \\ 0, r \leq \bar{x}_i^k \leq L-r \\ -L, \bar{x}_i^k \geq L-r \end{cases} \quad (6)$$

$$\bar{x}_i^{k'} = \bar{x}_i^k + \lambda_i^k \quad (7)$$

where  $\bar{x}_i^{k'}$  represents the coordinates of the new generated sphere,  $\lambda_i^k$  is the correction parameter that is determined comprehensively by  $\bar{x}_i^k$ , cross-sectional size of RVE  $L$ , and fiber radius  $r$ . For spheres in the boundary of RVE (blue spheres in Figure 3), the new sphere is generated at the symmetrical position of RVE. For the spheres located at the four corners of the plane (red spheres in Figure 3), the coordinates these spheres are simultaneously adjusted to ensure periodicity. By sequentially setting the periodicity conditions of the spheres in each plane, the geometric periodicity of the soft-core fiber system can be ensured.

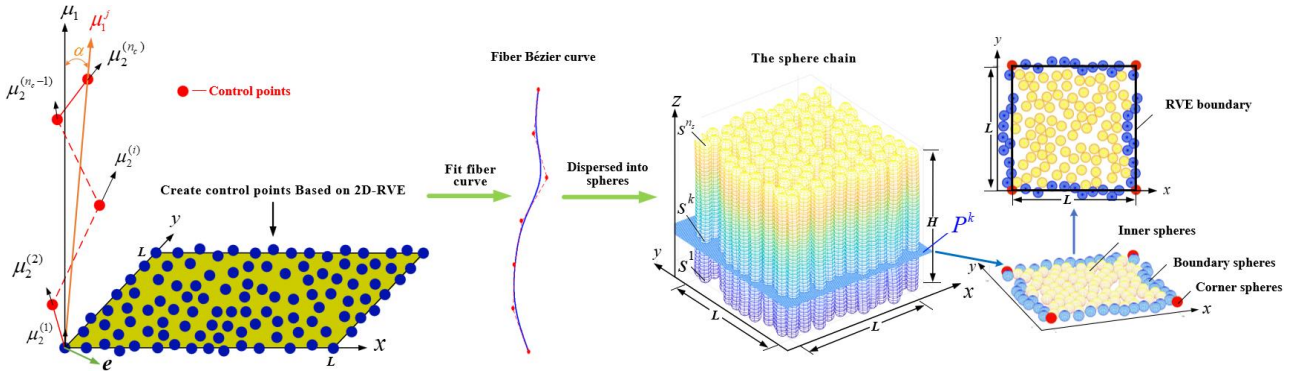


Fig. 3. The process of fiber misalignment generation

The experimentally determined angle values of fiber misalignment in UD-FRP range from  $-5^\circ$  to  $5^\circ$  [32], which can be statistically characterized by setting the reliability parameters  $k_1 = 1$  and  $k_2 = 300$  of the multivariable von Mises Fischer distribution when fitting the probability statistical distribution of angle deviation values [37]. Based on this, given a standard value of  $k_1 = 1$ , the Bézier curve of different fiber misalignments can be created by setting the reliability parameter  $k_2 = 100, 300$  and  $500$ , respectively.

To avoid the overlap between fibers, a force-bias algorithm, which acts on the sphere chain



dispersed by fiber curves, is applied to eliminate the overlap between fibers on the premise that the configuration of the fibers is basically unchanged. The implementation details of the force-bias algorithm can be found in [37].

### 2.1.3. Micro-voids in the matrix

Many studies have stated that the intra-laminar voids in UD-FRP have cylindrical morphology and elliptic cross-section that run along the fibers with a large average length-to-radius ratio. Almost no void developments were observed in the direction perpendicular to the fibers [8, 23, 24, 38]. For the sake of simplicity, the micro-voids are assumed to have circular cross-sections and sufficient lengths larger than the RVE along the fiber direction in this study.

Previous studies pointed out that the ultimate strain of UD-FRP increases with the increasing average value of micro-void radius. Such an effect is no longer significant when the radius reaches 0.15 times of the fiber diameter  $d_f$  [21, 24]. Therefore, the average micro-void radius in this study is  $0.15d_f$ , and the Gaussian distribution parameters are taken as  $\mu = 0.15d_f$  and  $\sigma^2 = 0.3 \mu\text{m}^2$ .

The first step is to generate the randomly distributed circular voids in the 2D-RVE domain, and their radius  $r_v$  follows Gaussian distribution. The intersection between them is checked using Ergodic contact formula as follows:

$$C_m = \sqrt{(x_i - x_m)^2 + (y_i - y_m)^2} - (r_i + r_m) \quad m = 1, 2, \dots, i-1 \quad (8)$$

where  $C_m$  is the contact determination factor. It represents the compatibility between the current micro-void  $(x_i, y_i)$  and all the existing micro-voids  $(x_m, y_m)$ . For every position of micro-void generated, an intersection check is performed; if the new position does not overlap with any of the existing micro-voids, the new position is accepted; otherwise, it is discarded.

The created 2D void geometry is stretched along the longitudinal direction of RVE to generate the 3D void geometry. Finally, the comprehensive RVE that includes geometrical fiber arrangement, fiber misalignment, and micro-voids can be obtained by applying Boolean operations to the fiber and void geometry, as shown in Figure 4.

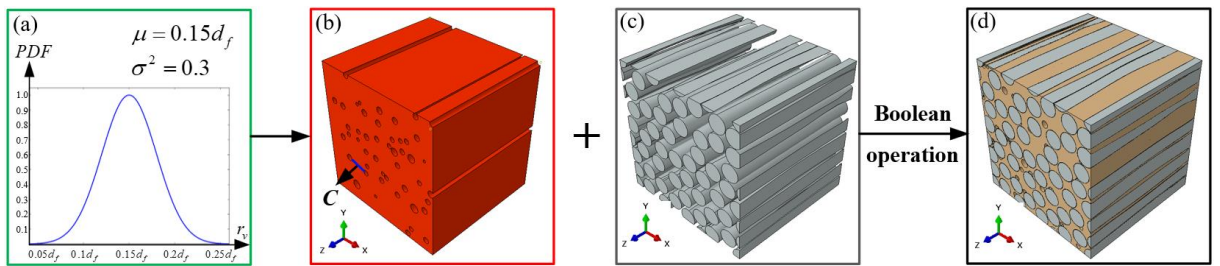


Fig. 4. Generation process of RVE containing three kinds of micro defects; (a) 2D micro-voids creation with radius following Gaussian distribution; (b) the 3D micro-voids model; (c) the fiber model with the random arrangement and fiber misalignment; (d) the RVE containing three kinds of micro-defects

## 2.2. Constitutive material models

The above-mentioned geometric RVE has been produced using various parameters for geometrical fiber arrangement, fiber misalignment, and micro-voids. The micro-modeling involves three constituents: carbon fibers, epoxy matrix, and fiber-matrix interface. The corresponding constitutive models and material parameters in this study are assigned by assuming the T800H/AC531 composite.

### 2.2.1. Carbon fibers

The considered loadings usually cannot cause fiber breakage, so only the linear elastic stage is taken into account for the carbon fibers. The transversely isotropic model is used with material properties listed in Table 2.

Table 2. Material properties of T800H carbon fibers [39]

Parameter	Symbol	Value
Fiber diameter ( $\mu\text{m}$ )	$d_f$	9
Longitudinal Young's modulus (MPa)	$E_1$	294000
Transverse Young's modulus (MPa)	$E_2 = E_3$	14000
Longitudinal Poisson's ratio	$\nu_{12} = \nu_{13}$	0.23
Transverse Poisson's ratio	$\nu_{23}$	0.25
Longitudinal shear modulus (MPa)	$G_{12} = G_{13}$	15000
Transverse shear modulus (MPa)	$G_{23}$	5500

### 2.2.2. Epoxy matrix

The epoxy matrix behaves isotropically and fails at a relatively low strain in a brittle manner under tensile loading but can undergo considerable plasticity and progressive damage under compressive or shear loading. Besides, plastic yielding and flow stress are sensitive to hydrostatic pressure [40]. This study adopts the extended Drucker-Prager yield criterion and linear hardening for the available in Abaqus, which is defined as:

$$F = t - p \tan \beta - d = 0 \quad (9)$$

where  $p$  is hydrostatic pressure,  $\beta$  is friction angle,  $d$  is the cohesion of resin matrix,  $t$  is yield shear stress, all of which are given as:

$$\sin \varphi = \frac{\sigma_c - \sigma_t}{\sigma_c + \sigma_t} \quad (10)$$

$$p = -\text{trace}(\sigma) / 3 \quad (11)$$

$$\beta = \tan^{-1} \left( \frac{6 \times \sin \varphi}{3 - \sin \varphi} \right) \quad (12)$$

$$d = \left( \frac{1}{k} + \frac{1}{3} \tan \beta \right) \sigma_t \quad (13)$$

where  $\sigma_t$  and  $\sigma_c$  represent the tensile strength and compressive strength of the material,  $\varphi$  is the friction angle in the corresponding Mohr-Coulomb model, and  $k$  represents the ratio of triaxial tensile yield stress to triaxial compressive yield stress:

$$k = \frac{3 - \sin \varphi}{3 + \sin \varphi} \quad (14)$$

Then the yield shear stress  $t$  is given as:

$$t = \frac{1}{2} q \left[ 1 + \frac{1}{k} - \left( 1 - \frac{1}{k} \right) \left( \frac{J_3}{q} \right)^3 \right] \quad (15)$$

where  $q$  represents the Mises equivalent stress, and  $J_3$  represents the third invariant of the partial stress tensor.



The existing experimental results show that AC531 epoxy resin has an obvious yielding and plastic deformation under compressive loading, as shown in Figure 5(a). The ductile damage model built in Abaqus was used to define the damage initiation and evolution of the resin matrix. The properties of AC531 epoxy resin are shown in Table 3.

Table3. Material properties of AC531 epoxy resin [39]

Parameter type	Symbol	Value
Young's modulus (MPa)	$E$	4740
Poisson's ratio	$\nu$	0.38
Tensile yield stress (MPa)	$\sigma_{t0}$	48
Tensile strength (MPa)	$\sigma_t$	65
Compressive strength (MPa)	$\sigma_c$	131
Friction angle ( $^{\circ}$ )	$\beta$	37.7
Flow stress ratio	$K$	0.8
Tensile fracture strain	$\varepsilon_{0,t}^p$	0.025
Compressive fracture strain	$\varepsilon_{0,c}^p$	0.25
Fracture energy (J/m <sup>2</sup> )	$G_{IC}$	1

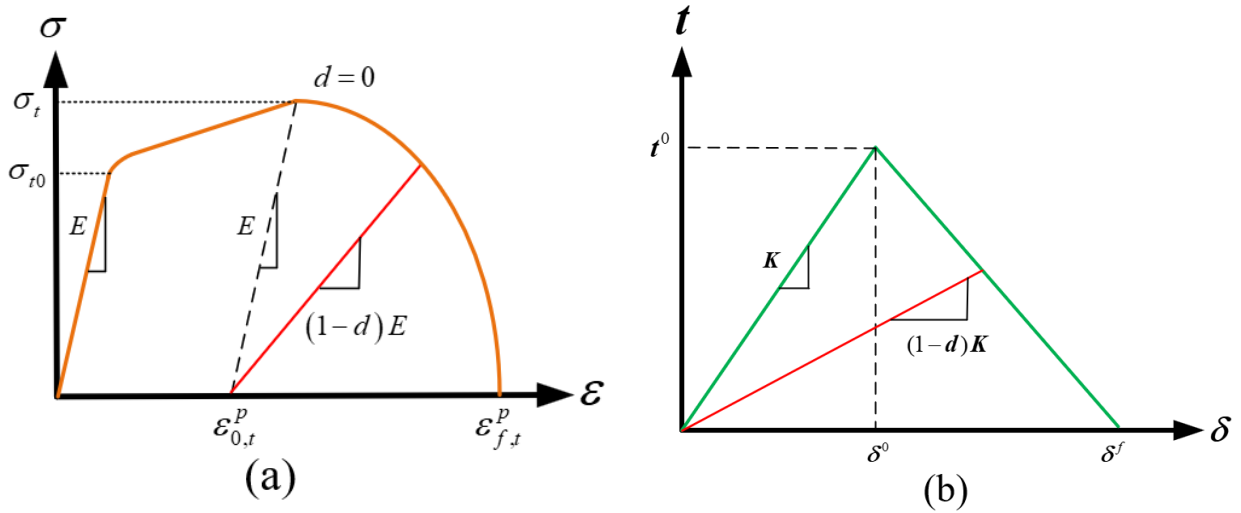


Fig.5. The damage evolution law for the (a) polymer matrix and (b) cohesive interface

### 2.2.3. Fiber–matrix interface

The interface between fiber and matrix is modeled by the cohesive model. Here, the bilinear traction separation law is used to characterize the cohesive damage, as shown in Figure 5(b). In the initial elastic stage, under the constant stiffness matrix, the traction force increases linearly with the separation. When the load increases to the critical strength of the interface, damage occurs, the stiffness matrix deteriorates linearly, and the bearing capacity of the interface continues to weaken until it disappears completely.

The initial linear-elastic behavior is given as:

$$\mathbf{t} = \begin{bmatrix} t_n \\ t_s \\ t_t \end{bmatrix} = \mathbf{K} \boldsymbol{\delta} = \begin{bmatrix} K_n & 0 & 0 \\ 0 & K_s & 0 \\ 0 & 0 & K_t \end{bmatrix} \begin{bmatrix} \delta_n \\ \delta_s \\ \delta_t \end{bmatrix} \quad (16)$$

where  $\mathbf{t}$  and  $\boldsymbol{\delta}$  are stress and displacement vectors,  $\mathbf{K}$  is the stiffness matrix, with the subscript  $n$  for normal direction and  $s/t$  for tangential directions. The stiffness settings of  $K_n$  and  $K_{s/t}$  are suitable for the stress continuity of the interface before damage. In addition, the damage initiation is determined by the quadratic nominal traction criterion:

$$\left( \frac{\langle t_n \rangle}{t_n^0} \right)^2 + \left( \frac{t_s}{t_s^0} \right)^2 + \left( \frac{t_t}{t_t^0} \right)^2 = 1 \quad (17)$$

where  $\langle \rangle$  represents Macaulay parentheses,  $t_n^0$ ,  $t_s^0$  and  $t_t^0$  represent critical normal strength, in-plane shear strength and out-plane shear strength, respectively. Once the damage initiation criterion is satisfied, the fiber-matrix debonding begins. Through a single normalized scalar damage variable, the cohesive tractions transmitted through the interface decrease linearly to zero. The fracture energy dependence on the mode mixity is defined by the Benzeggagh-Kenane damage propagation criterion, and the fracture energy required for complete interface failure is defined by  $G_n$  and  $G_s$ :

$$G^C = G_n^C + \left( G_s^C - G_n^C \right) \left( \frac{2G_s}{G_n + 2G_s} \right)^{\eta_{BK}} \quad (18)$$

where  $G_n$  and  $G_s$  are the normal and shear fracture energies, respectively.  $G^C$  is the corresponding critical fracture energy, and  $\eta_{BK}$  is the Benzeggagh-Kenane parameter. Because the critical value of fracture energy is difficult to measure experimentally, it is generally considered that a lower value can capture the brittle behavior of unidirectional composites under transverse tension. The interface parameters are listed in Table 4.

Table 4. Material properties of T800/AC531 interface [39]

Parameter	Symbol	Value
Normal elastic stiffness (MPa/mm)	$K_n$	$10^8$
Shear elastic stiffness (MPa/mm)	$K_s$	$10^8$
Normal maximum traction (MPa)	$t_n^0$	52
Shear maximum traction (MPa)	$t_s^0$	52
Normal fracture toughness (N/mm)	$G_n^C$	0.004
Shear fracture toughness (N/mm)	$G_s^C$	0.008

### 2.3. Model size, mesh, and boundary conditions

After involving the considered micro-defects, a set of RVEs with the same radius fiber were generated for micromechanical analysis. Existing studies have shown that a total of about 50 fibers of RVEs are sufficient to fully capture the basic characteristics of the material microstructure [41]. In the literature, there are many recommendations for determining the RVE cross-sectional size  $L$ , mainly based on the analysis of the transverse loading, such as  $L/d_f = 3\sim 7$  [42],  $L/d_f = 6$  [43], and  $L/d_f = 15$  [44]. Meanwhile, Sebaey et al. discussed that the strength under longitudinal loading shows up to 5% deviation when the RVE cross-sectional size is 8 times the fiber diameter, and the stiffness does not differ from the results with a larger RVE [17]. Based on this solution, the cross-sectional

size  $L = 8d_f$  is considered suitable for the numerical calculation under various load forms of this study. The target RVE has 63 fibers with a fiber diameter of  $d_f = 9 \mu\text{m}$  and a volume fraction of  $v_f = 58.9\%$ , resulting in a cross-sectional size of  $L = 72 \mu\text{m}$ . An example of generated RVE is shown in Figure 6.

For the sake of computation convergence, all the simulations were carried out with Abaqus/Explicit within the framework of the finite deformation theory. The micro model had 4-node linear tetrahedron elements (C3D4) with hourglass control for the fiber and matrix and 6-node three-dimensional cohesive elements (COH3D6) for the interface. In addition, the element deletion was triggered to avoid excessive distortion during loading.

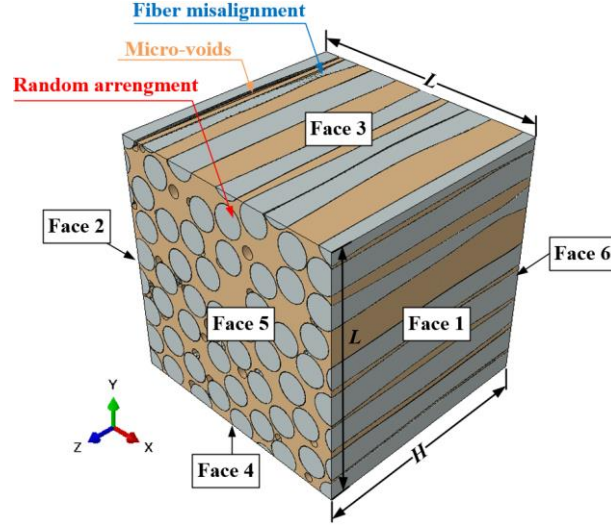


Fig. 6. Micro-defects features and face identification of the developed RVE

The applied boundary conditions on RVE can affect the calculated overall mechanical properties [45]. The widely used periodic boundary conditions (PBCs) introduce a priori constraint on the fiber kink-band during longitudinal compression [46], which may lead to overestimating the longitudinal mechanical properties. Combined with the consideration of computational cost, the final model applied kinematic uniform boundary conditions (KUBCs) with the specific settings as follows.

(i) Longitudinal compression:  $\varepsilon_c^{11}$  represents the compressive strain along the longitudinal direction of RVE (Z-direction), which is determined as 0.07 in this study. The boundary conditions are given as:

$$\begin{cases} u_z^{Face6} = u_y^{Face6} = 0 \\ u_z^{Face5} = \varepsilon_c^{11} \cdot H \end{cases} \quad (19)$$

(ii) Transverse tension/compression:  $\varepsilon_t^{22}$  and  $\varepsilon_c^{22}$  represent the tensile and compressive strains along the transverse direction (X-direction) of the RVE, respectively, which are determined as 0.008 and 0.03 in this study. The boundary conditions are given as:

$$\begin{cases} u_x^{Face2} = 0 \\ u_x^{Face1} = \varepsilon_{t/c}^{22} \cdot L \end{cases} \quad (20)$$

(iii) Transverse shear:  $\varepsilon_s^{23}$  represent the applied transverse shear strains of the RVE, which is determined as 0.004 in this study. The boundary conditions are given as:

$$\begin{cases} u_y^{Face1} = u_x^{Face4} = \varepsilon_s^{23} \cdot L \\ u_y^{Face2} = u_x^{Face3} = -\varepsilon_s^{23} \cdot L \\ u_z^{RP} = 0 \end{cases} \quad (21)$$

(iv) Longitudinal shear:  $\varepsilon_s^{12}$  represent the applied longitudinal shear strains of the RVE, also determined as 0.004 in this study. The boundary conditions are given as:

$$\begin{cases} u_z^{Face3} = \varepsilon_s^{12} \cdot L \\ u_z^{Face4} = -\varepsilon_s^{12} \cdot L \\ u_y^{Face3} = u_x^{Face4} = 0 \end{cases} \quad (22)$$

(v) Combined transverse tension/compression and longitudinal compression: Different proportions of strain  $\varepsilon_c^{11}/\varepsilon_t^{22} = 0, 1, 1.5, 2, 10, \infty$  and  $\varepsilon_c^{11}/\varepsilon_c^{22} = 0, 1, 1.5, 3, 5$  are applied to determine the biaxial load ratio, the boundary conditions are given as:

$$\begin{cases} u_z^{Face6} = u_x^{Face2} = 0 \\ u_z^{Face5} = \varepsilon_c^{11} \cdot H \\ u_x^{Face1} = \varepsilon_t^{22} \cdot L \end{cases} \quad (23)$$

A mesh dependency analysis is necessary to ascertain whether the selected mesh refinement is enough to ensure convergence. It has been checked for a high fiber misalignment level of  $k_2 = 100$  using five characteristic element lengths of  $S_m = d_f/3, d_f/4, d_f/5, d_f/6$  and  $d_f/8$ . The geometry for all computations remains the same, and only the mesh density was changed. Uniaxial compression along the fiber direction was applied on the generated RVE with the results plotted in Figure 7. Because a fine mesh could more accurately characterize the local stress concentration for the strain-softening material, the decrease in element size led to a prediction drop of the compressive strength. It was found that a characteristic element length of  $d_f/6$  ( $= 1.5 \mu\text{m}$ ) is necessary to obtain satisfying convergence. Consequently, this study adopted this mesh size throughout all the simulations. It should be noted that the mesh size is rather uniform across the domain, with the exception of regions where small geometric details must be captured by the mesh.

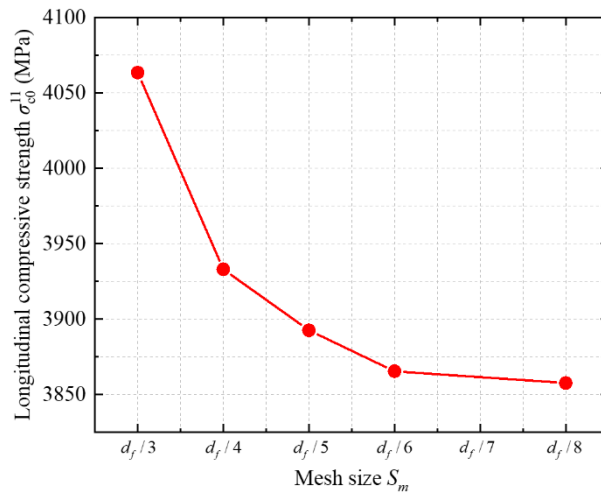


Fig. 7. Effect of mesh size on longitudinal compressive strength  $\sigma_c^{11}$ .

The size of the RVE in the fiber direction could cause fluctuations in the predicted longitudinal

response making it critical to select an appropriate value [18]. In this case, a series of longitudinal lengths of  $H = 0.5L$ ,  $0.75L$ ,  $1L$ ,  $1.5L$  and  $2L$  was used to examine the size dependence for a severe misalignment of the fibers,  $k_2 = 100$ . Using a workstation computer with an Intel Core i9-10900 CPU and 32 G of internal memory to calculate relevant cases, and uniaxial compression along the fiber direction was imposed with the effective strength and computational time plotted in Figure 8. The results show that the strength gradually drops with the size increase of RVE in the fiber direction. This is due to the fact that longer fibers are more likely to lose stability under longitudinal compression. Thus, when the longitudinal length of the RVE becomes smaller, the compressive strength approaches that of the RVE with straight fibers. It turns out that a length equal to the cross-sectional size, i.e.,  $H = L$ , is sufficient to obtain a reasonable convergence. The fluctuation of strength exhibits a relative change within 5% compared to a shorter RVE. Consequently, the cube RVE with a side length of  $72 \mu\text{m}$  is used for all studies throughout the paper.

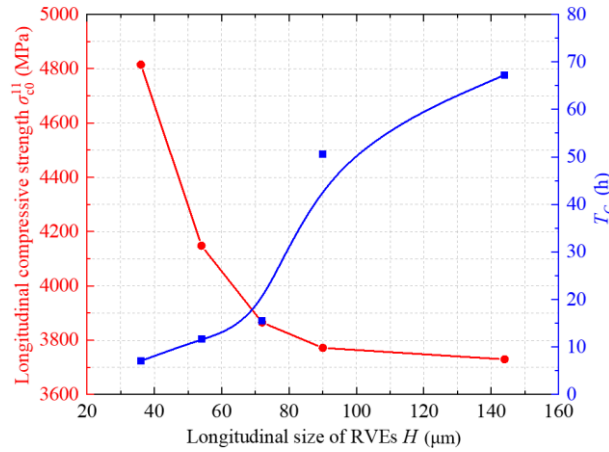


Fig. 8. Effect of longitudinal size of RVEs on longitudinal compressive strength  $\sigma_{00}^{11}$ , and CPU time  $T_c$ .

### 3. Influence of the individual defects

Table 5. Parameter setting of each micro-defect

Defect type	Geometric fiber arrangement	Fiber misalignment	Micro-voids contents
Parameter	Hexagonal arrangement	$k_2=\infty$ (Straight fiber)	$P_v=0$
		$k_2=500$	$P_v=0.6\%$
	Random arrangement	$k_2=300$	$P_v=1.8\%$
		$k_2=100$	$P_v=3.0\%$

The influence of the defects under the proposed loading set was analyzed by comparing the strength of the ideal RVE with the RVE including defects. To estimate how each kind of defect affects the strength of composites, the aforementioned defect-characterizing parameters were summarized in Table 5. The section included 38 test cases in total: two geometric fiber arrangements, four misalignment levels, and four micro-voids contents for five load cases. For each of the investigated microstructures defined by a unique parameter set, three RVEs were randomly generated to perform simulation and statistics.

#### 3.1 Effect of geometrical fiber arrangement

Two types of RVEs, namely hexagonal arrangement and random arrangement, were created to investigate the effect of fiber arrangements on the longitudinal compression properties of RVEs. Figure 9 compares their stress-strain curves under longitudinal compression. The main failure modes are fiber-matrix debonding and local matrix damage that occur simultaneously due to the Poisson effect of RVE under longitudinal compression. As the load increases, the local stress concentration

causes instability of fibers under compressive load, which leads to longitudinal RVE instability.

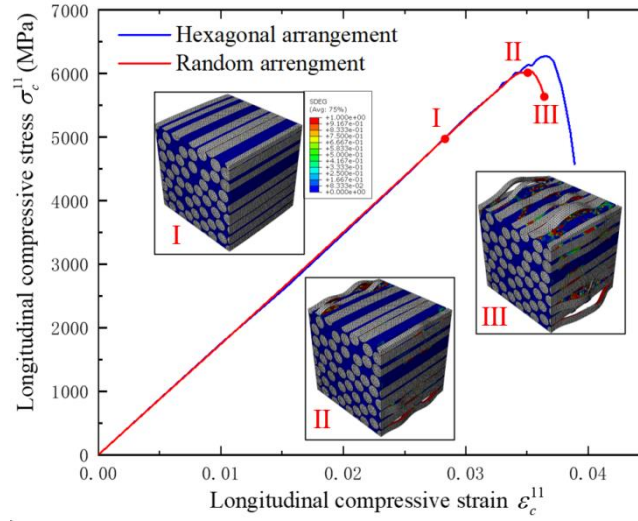


Fig. 9. The effect of different geometric fiber arrangements on longitudinal compression and corresponding damage forms.

The RVE with a hexagonal fiber arrangement exhibits higher damage strain and strength under longitudinal compression compared to the one with a random fiber arrangement. The difference in longitudinal compressive strength between the two fiber arrangements can reach 3.9%. The hexagonal arrangement prevents significant stress concentration that may result in instability of fibers. It is worth highlighting that within the RVE, the predominant cause of longitudinal compression damage stems from fiber buckling, matrix and interface failure. However, the occurrence of a fiber kink-band exhibits a size-dependent characteristic and necessitates a larger longitudinal size for the RVE to effectively capture this particular damage mode, which has consequently omitted in this study.

From the curve, the stiffness under longitudinal compression  $E_c^{11}$  is not affected by the geometric fiber arrangement because the RVE with different fiber arrangements has the same fiber deformation mode and the same fiber volume fraction in the linear elastic stage. To summarize, in the case of longitudinal compression, the hexagonal arrangement of fibers has a higher compressive strength than the random arrangement, but there is no significant difference in stiffness.

Figure 10(a) depicts the impact of different geometric fiber arrangements on the transverse tensile and compressive properties of RVEs. Compared with the hexagonal arrangement, the transverse tensile and compressive strength exhibits a decline with the random arrangement, attributable to the local stress concentration caused by small inter-fiber distances and the redistribution of maximum shear stress in the matrix.

Due to the influence of high local stress concentration, the transverse tensile damage strain of RVEs under the random arrangement is reduced by 13.9%, and the corresponding strength,  $\sigma_{t0}^{22}$ , is reduced by 4.0%, as shown in Figure 10(b-c). The transverse compression damage strain is also reduced by 12.7%, and the corresponding strength,  $\sigma_{c0}^{22}$ , is reduced by 8.0%. Similar to longitudinal compression, there is no significant difference in the stiffness of RVEs with different geometric fiber arrangements under a transverse load.

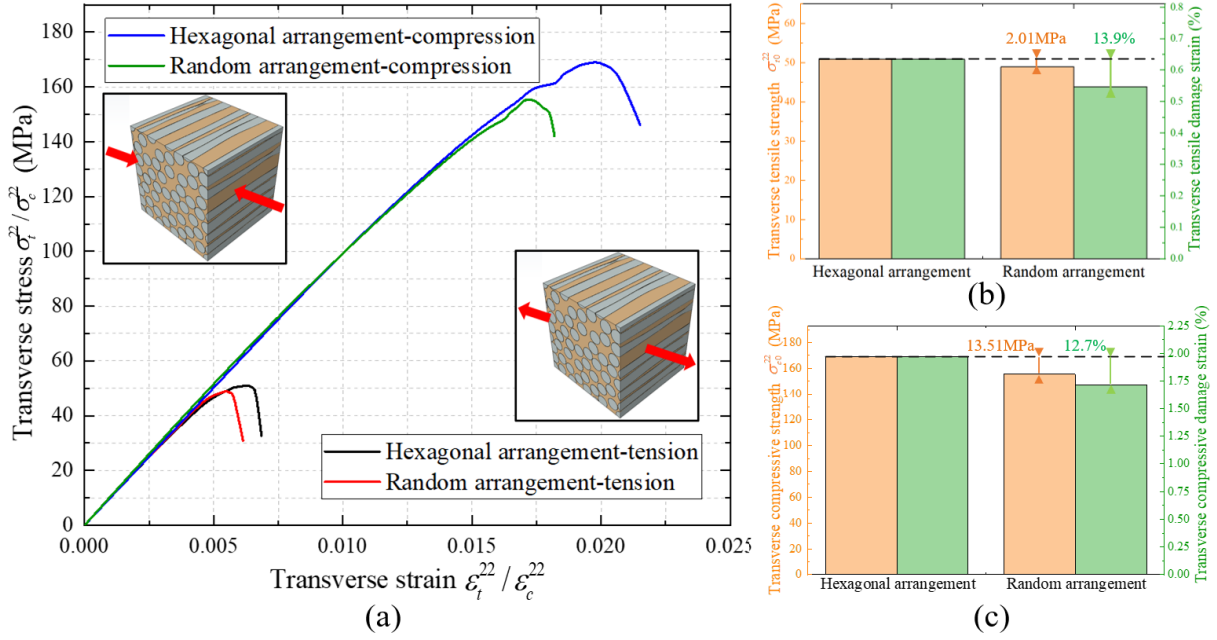


Fig. 10. The effect of geometric fiber arrangement on transverse tension and compression; (a) stress-strain curves; (b) numerical analysis of transverse tension; (c) numerical analysis of transverse compression

As for transverse and longitudinal shear, random fiber arrangement leads to earlier damage in RVEs, similar to the situation under transverse tension/compression, due to local stress concentration caused by small inter-fiber distances. It is worth noting that the random fiber arrangement has a negligible effect on the transverse shear strength  $\sigma_{s0}^{23}$  but a significant effect on the longitudinal shear strength  $\sigma_{s0}^{12}$ , as shown in Figure 11. Under transverse shear, the fiber-matrix debonding occurs before matrix damage, thus the overall load-bearing capacity of RVEs is relatively close. However, under longitudinal shear, fiber-matrix debonding and matrix damage occur simultaneously, resulting in significantly earlier occurrence of final damage, the random fiber arrangement significantly reduces the overall load-bearing capacity of RVEs.

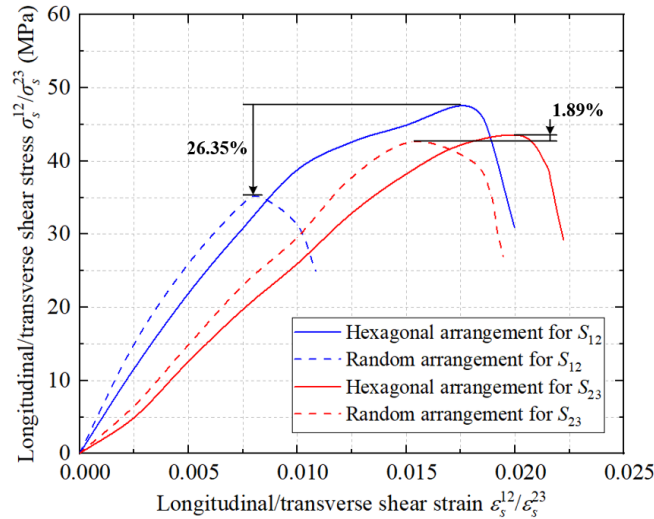


Fig. 11. The effect of geometric fiber arrangement on transverse shear  $S_{23}$  and longitudinal shear  $S_{12}$

### 3.2 Effect of fiber misalignment

Figure 12 shows the effects of different parameters of fiber misalignment on the longitudinal compression properties of RVEs. Four types of RVEs were generated with different parameters,



including  $k_2 = \infty$  (straight fiber), 500, 300, and 100. The stress-strain curves of these RVEs under longitudinal compression are shown in Figure 12(a). When UD-FRP undergoes longitudinal compression, the initial micro-buckling of the fiber facilitates the combination of shear stress transfer at the interface, which causes the debonding between the fiber and the matrix and the occurrence of the instability of fibers in advance. Additionally, the instability of fibers also accelerates further debonding between the fiber and the matrix, leading to a significant reduction in the final damage strength  $\sigma_{c0}^{11}$ . The difference in strength between the straight fiber ( $k_2 = \infty$ ) and high fiber misalignment ( $k_2 = 100$ ) can be as much as 30%.

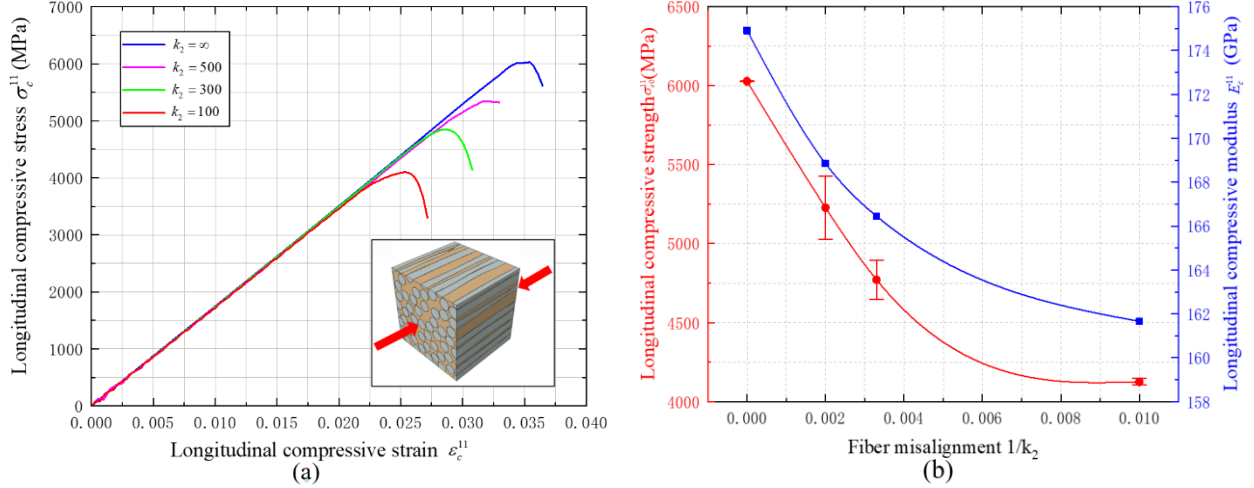


Fig. 12. The effect of fiber misalignment on longitudinal compression; (a) stress-strain curves; (b) numerical analysis

The longitudinal compression modulus  $E_c^{11}$  also decreases with the increase in fiber misalignment, although the effect is much smaller than that on strength. Figure 12(b) demonstrates a 6.5% difference in modulus between straight fiber and high fiber misalignment. In summary, fiber misalignment defects lead to a certain decrease in longitudinal compression strength and modulus.

For RVEs with the random fiber arrangement, Figure 13 shows that the difference in damage strain between straight fibers and high fiber misalignment under transverse tension is only 1.4%, and the difference in strength is only 0.2%. Under transverse compression, the difference between damage strain and strength is only 1.0% and 1.4%, respectively. In contrast to straight fiber, RVEs with fiber misalignment exhibit no anisotropy in their transverse stiffness. In conclusion, the mechanical properties of UD-FRP are not affected by fiber misalignment under transverse tension and compression. According to the finding of T.A. Sibey et al. [17], the transverse/longitudinal shear properties of UD-FRP are not affected by fiber misalignment. Therefore, this paper will not separately discuss the effect of fiber misalignment on shear properties.

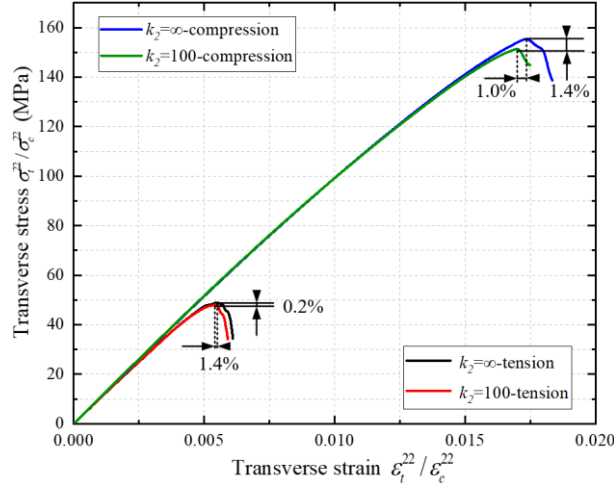


Fig. 13. The effect of fiber misalignment on transverse tension and compression

### 3.3 Effect of micro-voids

Figure 14 depicts the effect of different micro-void contents on longitudinal compression. Four types of RVE were generated with varying porosities of  $P_v = 0, 0.6\%, 1.8\%$ , and  $3\%$ . The predicted stress-strain curves under longitudinal compression are illustrated in Figure 14(a). Micro-voids cause a reduction in the longitudinal compressive strength of UD-FRP  $\sigma_{c0}^{11}$ . This decrease is not due to the reduction in cross-sectional area resulting from the existence of micro-voids. However, it is instead attributed to stress concentration in the voids and the reduction of the cohesive area between fiber and matrix, which results in a more straightforward occurrence of local interfacial debonding and instability of fibers. At a porosity of  $3\%$ ,  $\sigma_{c0}^{11}$  decreases by  $5.4\%$ , as shown in Figure 14(b).

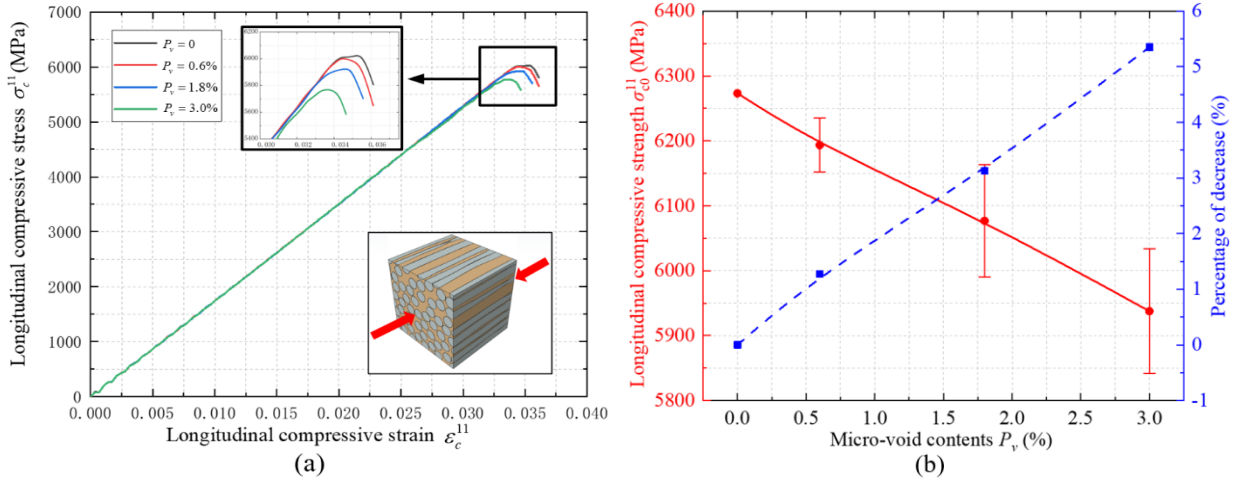


Fig. 14. The effect of micro-voids on longitudinal compression; (a) stress-strain curves; (b) numerical analysis

The impact of micro-voids on the longitudinal compression stiffness is negligible since the failure of RVEs happens almost immediately after the fiber and matrix debonding. Thus, any difference in modulus is only noticeable in a small loading section before the final damage ensues. Ultimately, micro-voids cause a marginal decrease in the longitudinal compressive strength  $\sigma_{c0}^{11}$ , but their influence on the longitudinal compressive stiffness  $E_c^{11}$  remains minimal.

Due to stress concentration near micro-voids, the matrix is more susceptible to plastic deformation and damage, which significantly impacts the transverse mechanical properties of UD-FRP. The effect mechanism has been discussed in numerous existing studies and will not be explored

further in this paper. For RVEs with randomly arranged fibers, 3% porosity results in a 28.1% reduction in the transverse tensile strength  $\sigma_{t0}^{22}$ , a 21.1% reduction in the corresponding damage strain, and a 17.9% reduction in Young's modulus  $E_t^{22}$ . It also significantly affects the transverse compression load, reducing the strength  $\sigma_{c0}^{22}$  by 29.3%, the damage strain by 22.8%, and Young's modulus  $E_c^{22}$  by 17.9%, as shown in Figure 15.

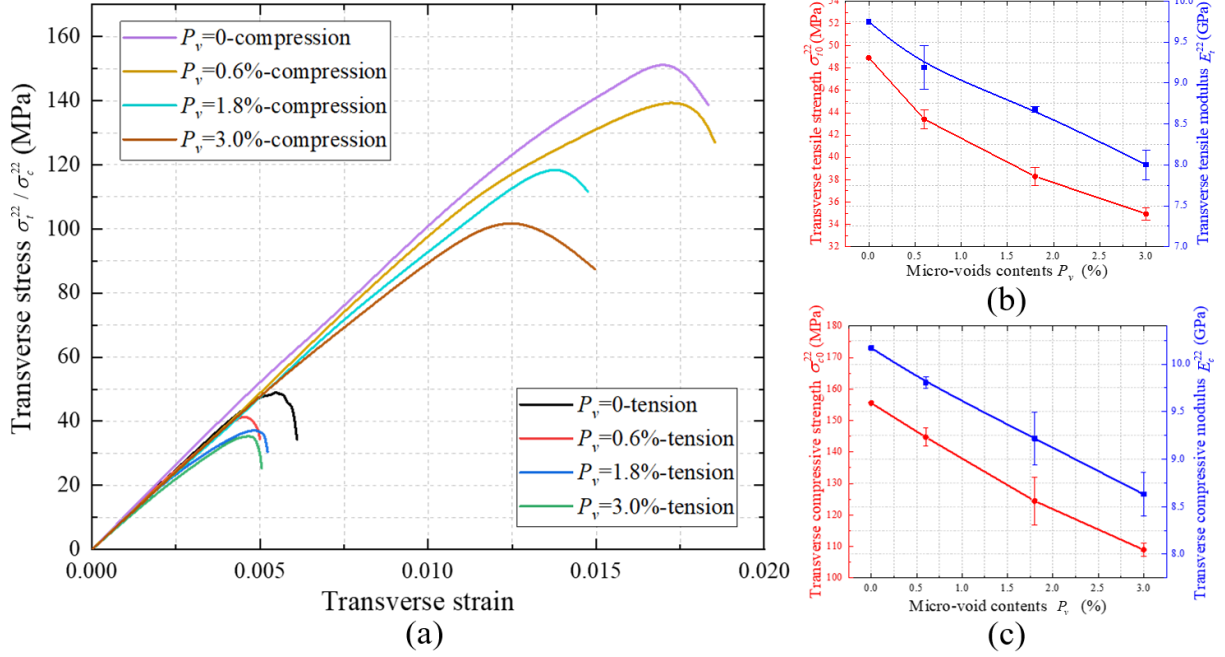
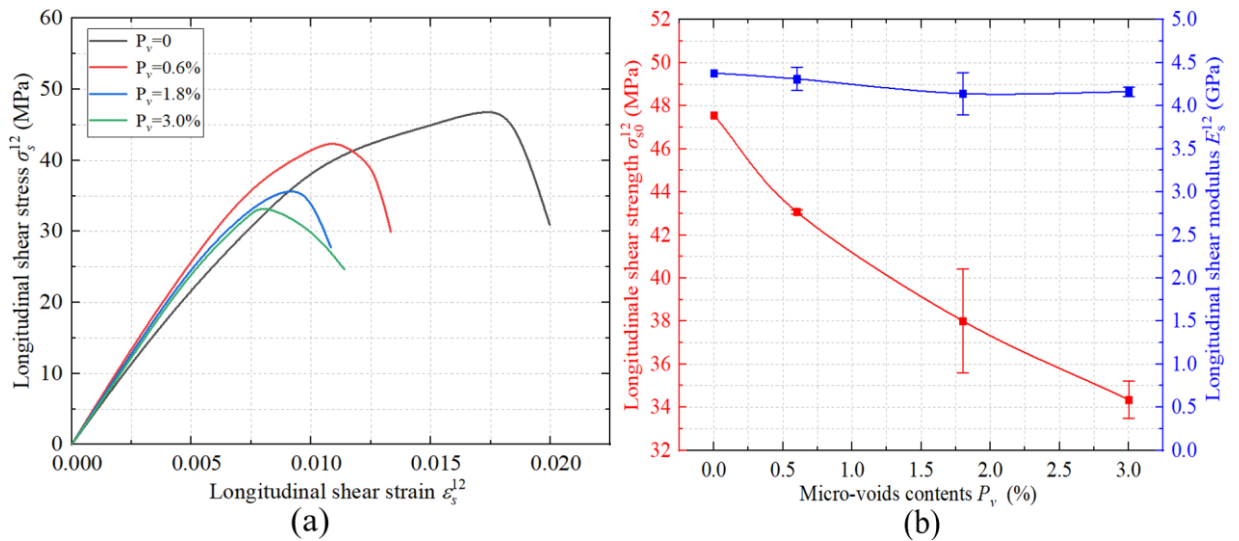


Fig. 15. The effect of micro-voids on transverse tension and compression; (a) stress-strain curves; (b) numerical analysis of transverse tension; (c) numerical analysis of transverse compression

Figure 16 shows the influence of micro-voids on transverse and longitudinal shear, and quantitatively analyzed the weakening effect of micro-voids on mechanical properties. Similar to the situation under transverse tension/compression, micro-voids significantly reduce the strength of transverse and longitudinal shear due to stress concentration near micro-voids. However, it can be observed that micro-voids have no significant effect on the transverse and longitudinal shear modulus  $E_s^{12} / E_s^{23}$ , which is different from the situation under transverse tension and compression.



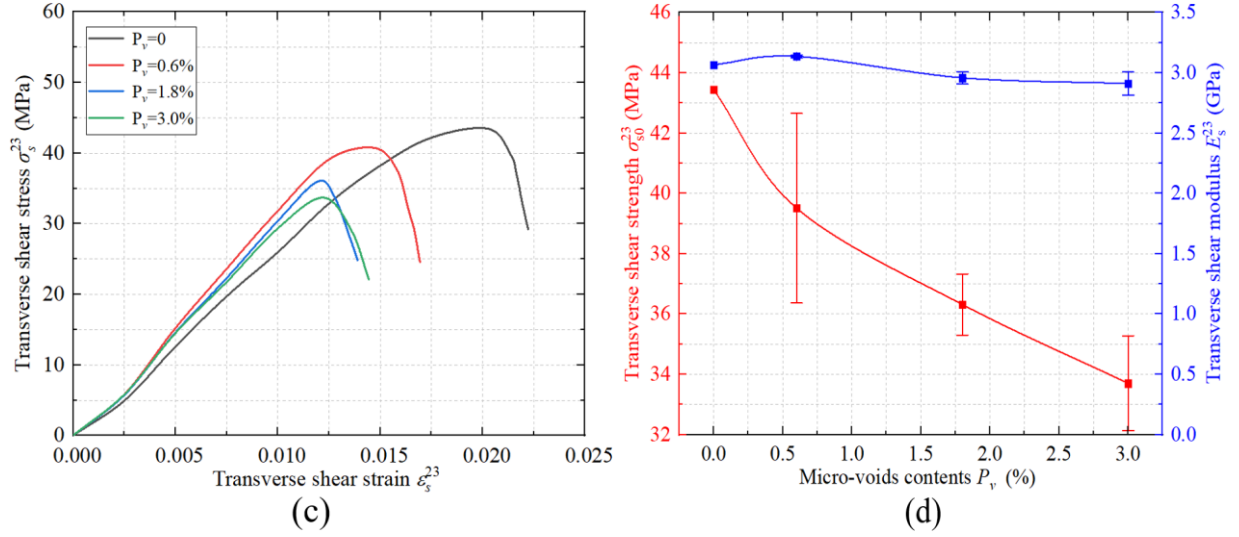


Fig. 16. The effect of micro-voids on transverse shear  $S_{23}$  and longitudinal shear  $S_{12}$ ; (a) stress-strain curves of longitudinal shear; (b) numerical analysis of longitudinal shear; (c) stress-strain curves of transverse shear; (d) numerical analysis of transverse shear

### 3.4 Summary of individual defect influence

Figure 17 presents a quantitative analysis of how random fiber arrangement, fiber misalignment, and micro-voids weaken the strength of the RVE under five different loading conditions: longitudinal compression, transverse tension/ compression, and transverse/ longitudinal shear. The results indicate a decrease in strength due to all three types of micro-defects, with fiber misalignment having the most significant impact on longitudinal compressive strength and micro-voids affecting transverse tensile and compressive strength the most, which aligns with previous studies. It is worth noting that negligence towards the impact of random fiber arrangement on all five loading conditions, and micro-voids on longitudinal compression, could prove disastrous.

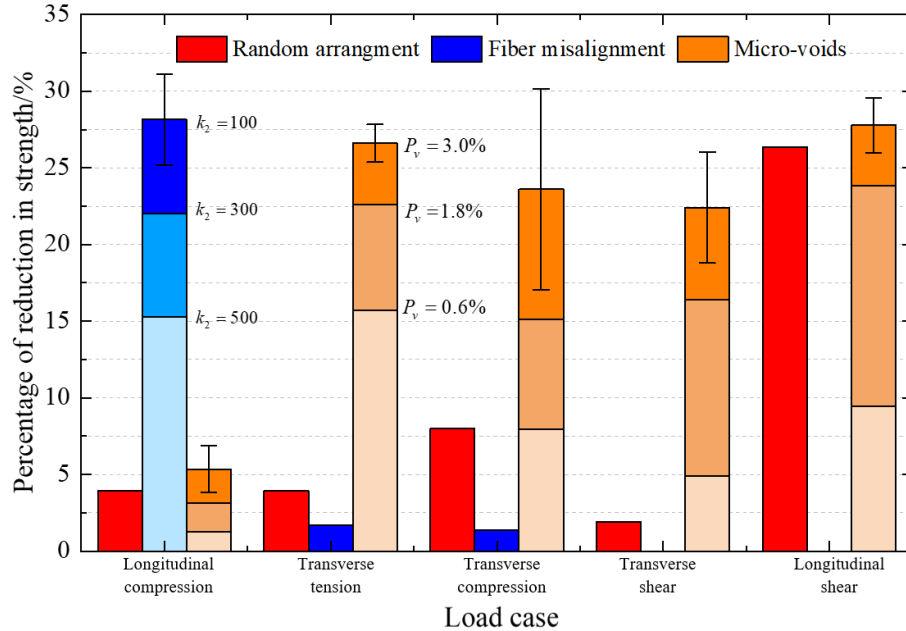


Fig. 17. The effect of random fiber arrangement, fiber misalignment, and micro-voids on the strength of RVE under five loading forms

## 4. Interaction of multiple defects

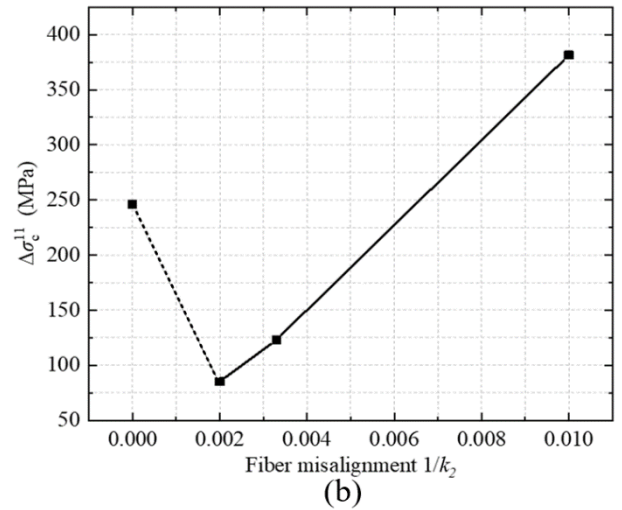
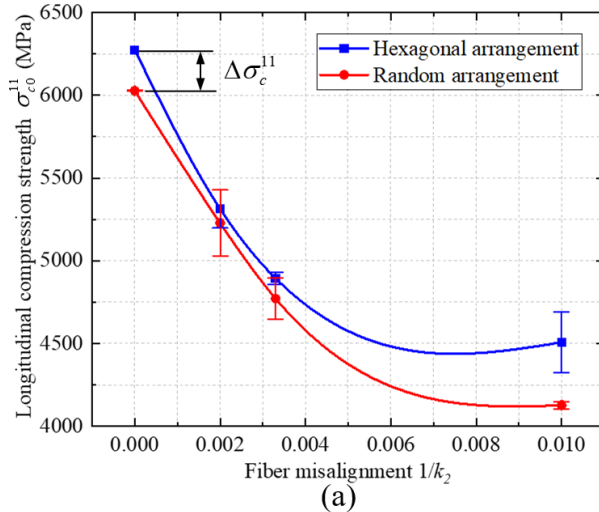
In order to gain insight into the correlation between geometric fiber arrangement, fiber misalignment, and micro-voids, a thorough full-factor analysis was conducted. RVEs containing diverse microscopic defects, characterized by different parameters, were assembled in accordance with the specifications outlined in Table 5. To ensure accuracy and consistency, a minimum of three RVEs were constructed and evaluated for each defect combination. By utilizing numerical calculations within a defined framework, the combined effects of the three micro-defects on the mechanical properties were analyzed under five loading modes: longitudinal compression, transverse tension/ compression, and transverse/ longitudinal shear.

### 4.1. Longitudinal compression

#### 4.1.1. Geometrical fiber arrangement and fiber misalignment

In order to investigate the interaction between geometric fiber arrangement and fiber misalignment, a total of 8 sets of RVEs were generated with fiber misalignment parameters of  $k_2=\infty$  (straight fibers), 500, 300, and 100 under the two different fiber arrangement forms. The coupling effects of the two defects on the longitudinal compression strength  $\sigma_{c0}^{11}$  are presented in Figure 18(a). It was observed that RVEs with the hexagonal fiber arrangement exhibited higher longitudinal compression strengths compared to those with the random fiber arrangement. This difference in strength was quantified as  $\Delta\sigma_c^{11}$ . Figure 18(b) illustrates the effect of different fiber misalignment parameters  $k_2$  on  $\Delta\sigma_c^{11}$ .

It has been identified that the longitudinal compression strength of UD-FRP is susceptible to fiber misalignment, with the strength of hexagonal arrangements being noticeably higher than that of random ones. As fiber misalignment increases in RVEs, there is a greater occurrence of local fiber micro-buckling, which subsequently lowers the minimum inter-fiber distances in RVEs of the random arrangement, causing further stress concentration of the matrix, as depicted in Figure 18(c). Conversely, RVEs with hexagonal arrangements have ample matrix volume around each fiber, leading to a negligible increase in stress concentration caused by local fiber micro-buckling. Ultimately, the influence of geometric fiber arrangement is amplified with greater fiber misalignment.





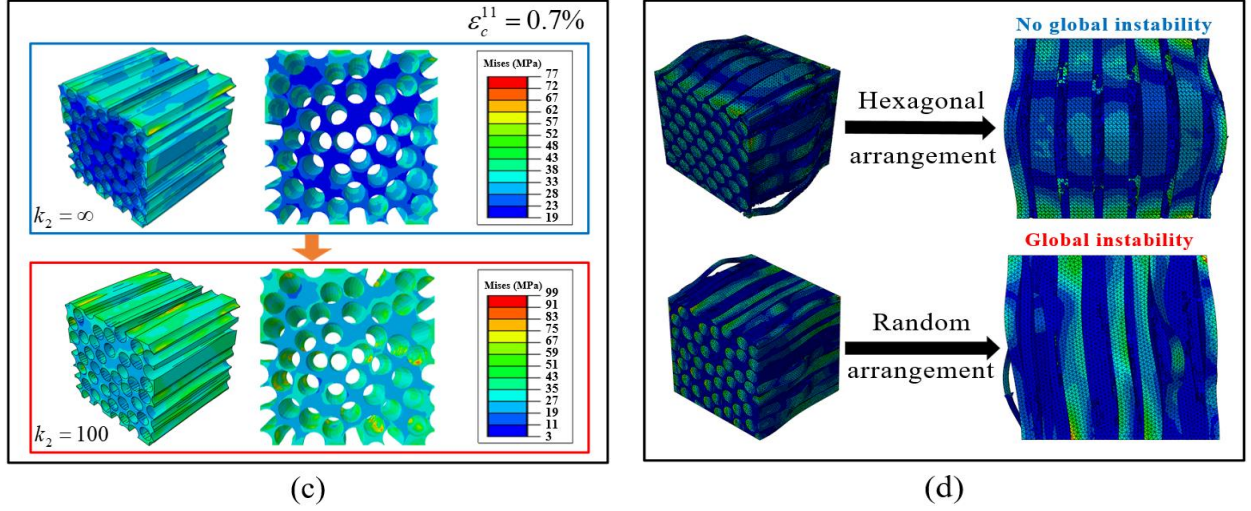
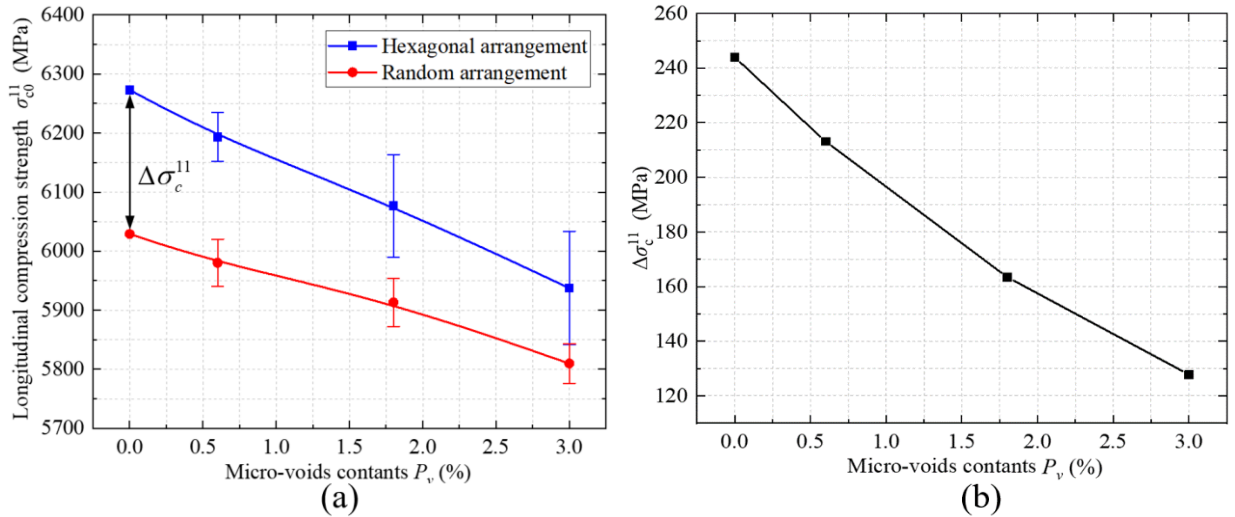


Fig. 18. The interaction between geometric fiber arrangement and fiber misalignment; (a) effect of  $k_2$  on  $\sigma_{c0}^{11}$  of RVEs in different fiber arrangements; (b) numerical result of the interaction; (c) the stress concentration of RVEs in  $k_2 = \infty$  and  $k_2 = 100$ ; (d) different final damage mode of the RVEs in different fiber arrangements

It is of noteworthy significance that when examining RVEs composed of straight fibers ( $k_2 = \infty$ ), they do not comply with the aforementioned interactions. This is due to the absence of global instability present in the ultimate pattern of damage exhibited in the hexagonal arrangement of RVEs featuring straight fibers, as depicted in Figure 18(d), resulting in a marked increase in strength when compared to that of the random arrangement.

#### 4.1.2. Geometrical fiber arrangement and micro-voids

In order to investigate the interaction between geometric fiber arrangement and micro-voids, a total of 8 sets of RVEs with micro-void contents of  $P_v = 0, 0.6\%, 1.8\%$ , and  $3\%$  were generated under the two different fiber arrangement forms. The coupling effect of the two defects on longitudinal compression strength  $\sigma_{c0}^{11}$  is shown in Figure 19(a). An increase in porosity leads to a decrease in the difference in longitudinal compressive strength under different fiber arrangements  $\Delta\sigma_c^{11}$ , and the effect is quantified in Figure 19(b).



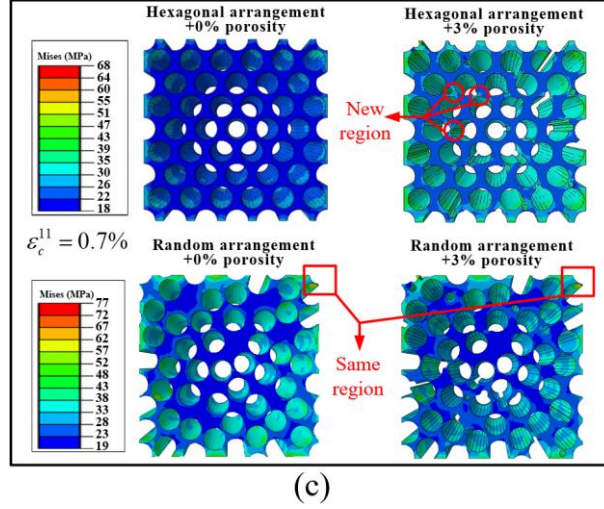


Fig. 19. The interaction between geometric fiber arrangement and micro-voids; (a) effect of  $P_v$  on  $\sigma_{c0}^{11}$  of RVEs in different arrangements; (b) numerical result of the interaction; (c) the stress concentration of RVEs in  $P_v=0$  and  $P_v=3\%$  under different fiber arrangement

As porosity increases, the longitudinal compressive strength decreases. Moreover, the strength of both geometric fiber arrangements tends to become similar with increased porosity, which means that  $\Delta\sigma_c^{11}$  gradually decreases as  $P_v$  increases. For the RVEs with a random arrangement, the minimum inter-fiber distances and maximum stress concentration points in the matrix remain constant. Conversely, the hexagonal arrangement RVEs are more susceptible to damage initiation caused by micro-voids. Since micro-voids create numerous small inter-fiber distances in hexagonal RVEs, new stress concentrations arise, as shown in Figure 19(c). Ultimately, micro-voids mitigate the influence of geometric fiber arrangement on longitudinal compression strength.

#### 4.1.3. Fiber misalignment and micro-voids

In order to investigate the interaction between fiber misalignment and micro-voids, a total of 16 sets of RVEs were generated with micro-void contents of  $P_v = 0$  and 3% and fiber misalignment of  $k_2 = \infty$  (straight fiber), 500 300 and 100 under the two fiber arrangement forms. The coupling effect of the two defects on longitudinal compression strength is shown in Figure 20(a).

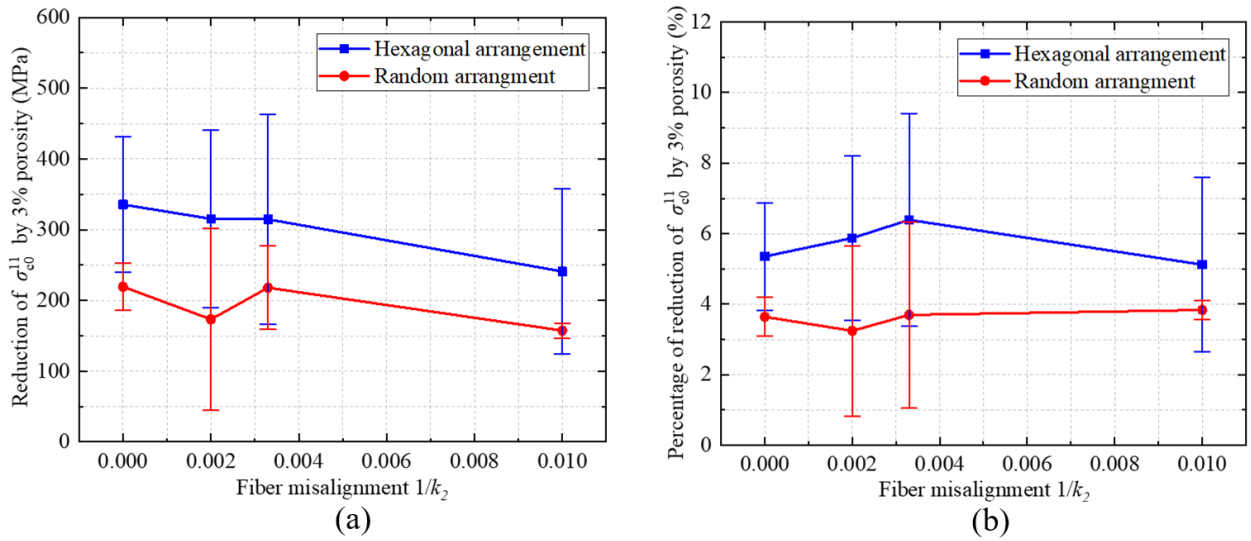


Fig. 20. The interaction between fiber misalignment and micro-voids; (a) effect of  $k_2$  on reduction of  $\sigma_{c0}^{11}$  by  $P_v=3\%$ ; (b) effect of  $k_2$  on percentage of reduction of  $\sigma_{c0}^{11}$  by  $P_v=3\%$



RVEs with different porosity have the same damage mode. To optimize computational efficiency when dealing with RVEs containing various micro-defects, the study is limited to a 3% porosity. Figure 20(b) quantifies the percentage reduction in longitudinal compressive strength with  $P_v = 3\%$  under different fiber misalignment parameters.

Regardless of the geometric fiber arrangement, fiber misalignment and micro-voids do not significantly interact with each other. That is, the weakening effect of porosity on the longitudinal compressive strength remains unaffected by the presence of fiber misalignment defects.

#### 4.1.4. Comprehensive influence of three kinds of micro-defects

In order to investigate the interaction among the three types of micro-defects, 16 sets of RVEs were generated with fiber misalignment parameters of  $k_2 = \infty, 100$  and micro-void contents of  $P_v = 0, 0.6\%, 1.8\%$  and  $3\%$  under the two fiber arrangement forms. Figure 21(a) shows the effect of porosity on the longitudinal compressive strength  $\sigma_{c0}^{II}$  under high fiber misalignment  $k_2 = 100$ .

The effect of lower fiber misalignment can be fully characterized by high fiber misalignment. To optimize computational efficiency, only straight fiber  $k_2 = \infty$  and high fiber misalignment  $k_2 = 100$  are considered. Figure 21(b) illustrates the effect of different porosities on straight fiber and high fiber misalignment, respectively.

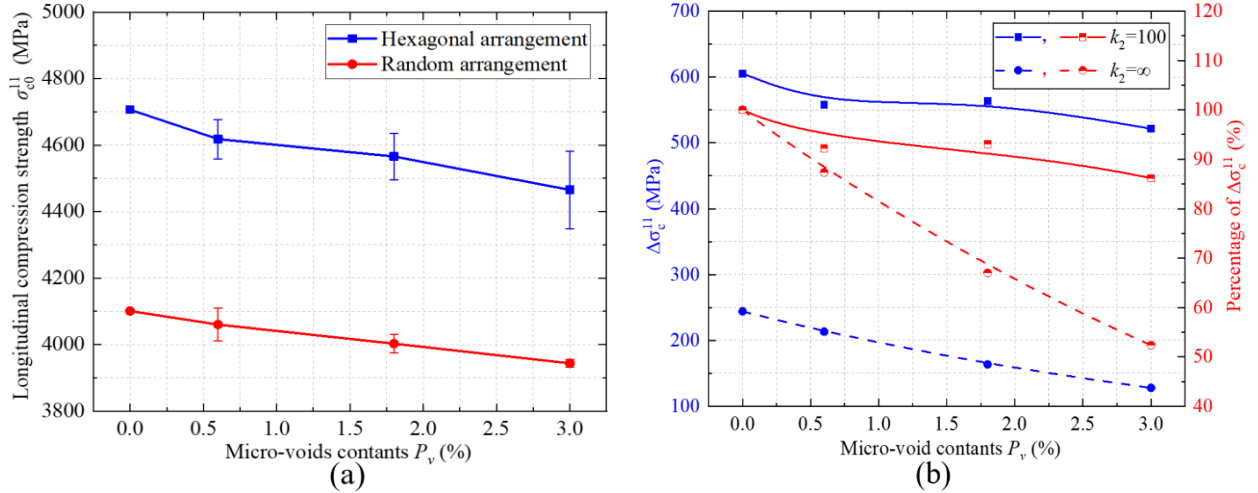


Fig. 21. The interaction between three kinds of micro-defects; (a) the effect of  $P_v$  on  $\sigma_{c0}^{II}$  of RVEs with  $k_2 = 100$  under different arrangements; (b) the effect of  $P_v$  on  $\Delta\sigma_c^{II}$  under different fiber misalignment

Obviously, the increase in porosity leads to a decrease in  $\sigma_{c0}^{II}$ . However, for RVEs with high fiber misalignment, the strength of the two types of fiber arrangement does not show an obvious trend toward an intersection. That is, for RVEs with straight fibers, a 3% porosity results in a 50% reduction compared to  $P_v = 0$ , while for RVEs with high fiber misalignment, the reduction is only 14%.

When fiber misalignment is not taken into account, the results in Section 4.1.2 show that micro-voids produce new stress concentrations in RVEs with a hexagonal arrangement, leading to the weakening effect of micro-void contents  $P_v$  on  $\Delta\sigma_c^{II}$ . However, the results in Section 4.1.1 show that fiber misalignment leads to an increase in stress concentration caused by the random arrangement of fibers, which leads to the enhancement of  $\Delta\sigma_c^{II}$ . In conclusion, despite the insignificant interaction between fiber misalignment and micro-voids, their impacts on geometric fiber arrangement are antagonistic.

#### 4.2. Transverse tension /compression

From Section 3.2, fiber misalignment does not have a significant effect on the transverse mechanical properties of UD-FRP. Therefore, only the interaction between geometric fiber arrangement and micro-voids is being examined

Figure 22 shows the impact of porosity on transverse tensile/compressive strength  $\sigma_{t0}^{22}$  and  $\sigma_{c0}^{22}$  with different geometric fiber arrangements. While RVEs with hexagonal arrangements exhibit higher strength compared to random arrangements, the strength difference  $\Delta\sigma_t^{22}$  and  $\Delta\sigma_c^{22}$  don't vary significantly as porosity increases. In summary, micro-voids do not impact  $\Delta\sigma_t^{22}$  and  $\Delta\sigma_c^{22}$ , and there is no significant interaction amongst geometric fiber arrangement, fiber misalignment, and micro-voids for the transverse mechanical properties of UD-FRP.

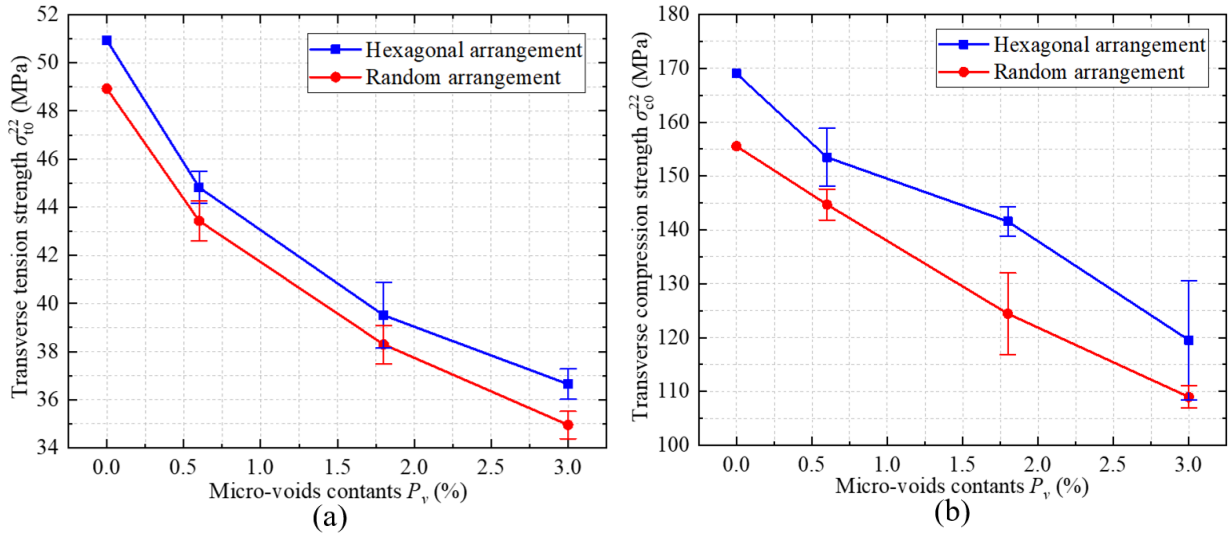


Fig. 22. The interaction between geometric fiber arrangement and micro-voids on transverse tension and compression; (a) effect of  $P_v$  on  $\sigma_{t0}^{22}$  of RVEs under different arrangements; (b) the effect of  $P_v$  on  $\sigma_{c0}^{22}$  under different arrangements

#### 4.3. Longitudinal/transverse shear

Figure 23 shows the impact of porosity on transverse/longitudinal shear strength  $\sigma_{s0}^{23}$  and  $\sigma_{s0}^{12}$  with different geometric fiber arrangements. For transverse shear, it can be observed that the geometric fiber arrangement has almost no effect on the strength  $\sigma_{s0}^{23}$ , that is, the transverse shear strength is only affected by porosity, and the strength difference  $\Delta\sigma_s^{23}$  don't vary significantly as porosity increases.

As porosity increases, the longitudinal shear strength decreases, and the strength of both geometric fiber arrangements tends to become similar with increased porosity, just like the trend under longitudinal compression, which means that  $\Delta\sigma_s^{12}$  gradually decreases as  $P_v$  increases, as shown in Figure 23(c). Since micro-voids create numerous small inter-fiber distances and stress concentration, damage occurs near micro-voids, which led to the hexagonal arrangement RVEs are more susceptible to damage initiation caused by micro-voids. For the RVEs with a random arrangement, the minimum inter-fiber distances and initial damage region in the matrix remain constant, as shown in Figure 23(d). Due to the impact caused by random fiber arrangement, the impact caused by micro-voids is not as significant as in the hexagonal arrangement RVEs. Ultimately, micro-voids mitigate the influence of geometric fiber arrangement on longitudinal shear strength.

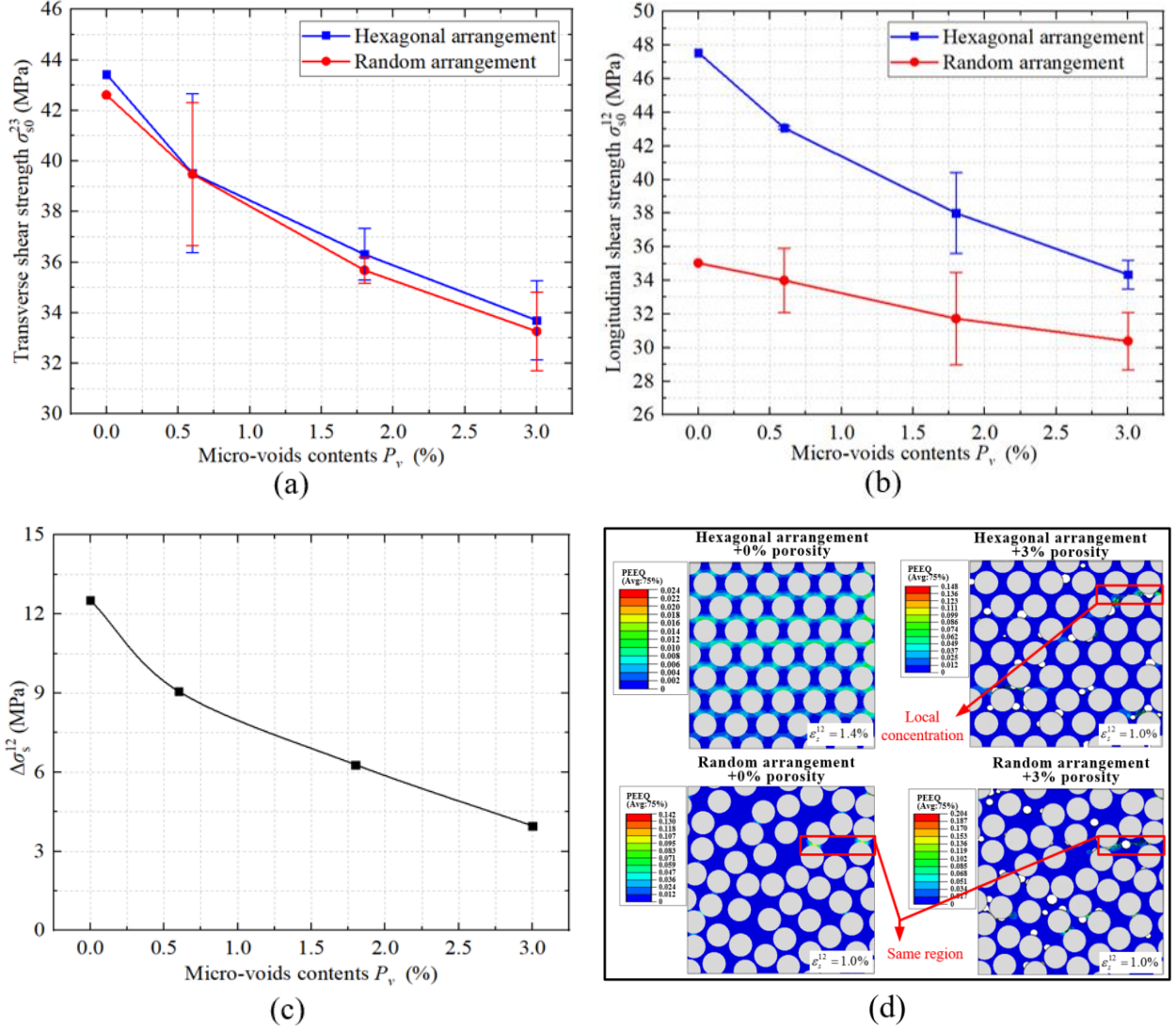


Fig. 23. The interaction between geometric fiber arrangement and micro-voids on transverse/ longitudinal shear; (a) effect of  $P_v$  on  $\sigma_{s0}^{23}$  of RVEs in different arrangements; (b) effect of  $P_v$  on  $\sigma_{s0}^{12}$  of RVEs in different arrangements; (c) numerical result of the interaction under longitudinal shear; (d) the damage analysis of RVEs in  $P_v=0$  and  $P_v=3\%$  under different fiber arrangement

#### 4.4. Biaxial load form

To thoroughly investigate the impact of geometric fiber arrangement, fiber misalignment, and micro-voids on the mechanical properties of UD-FRP subjected to biaxial loading, various combinations of longitudinal compression and transverse loads were applied to the two RVE configurations with the most significant differences. That is, the ideal RVE (hexagonal fiber arrangement, straight fibers  $k_2 = \infty$ , and no micro-voids  $P_v = 0$ ) versus the RVE with micro-defects (random fiber arrangement, high fiber misalignment  $k_2 = 100$ , and porosity  $P_v = 3.0\%$ ).

The biaxial damage envelope of two groups of RVEs is shown in Figure 24. When longitudinal or transverse damage occurs in RVEs, the RVEs are considered to have reached the final damage. The numerical results are compared to the predictions of the Tsa-Wu failure criteria under the corresponding configuration. For the failure strength under the combined longitudinal compression and transverse tension, the theoretical predictions of the ideal RVE are in good agreement with the results obtained from numerical simulations. However, the Tsai-Wu criteria slightly overestimated

the failure strength of the RVE with all three types of micro-defects. Meanwhile, the computational micromechanics-predicted strengths for both two configurations of RVE are slightly higher than the Tisa-Wu criteria for combined longitudinal and transverse compression.

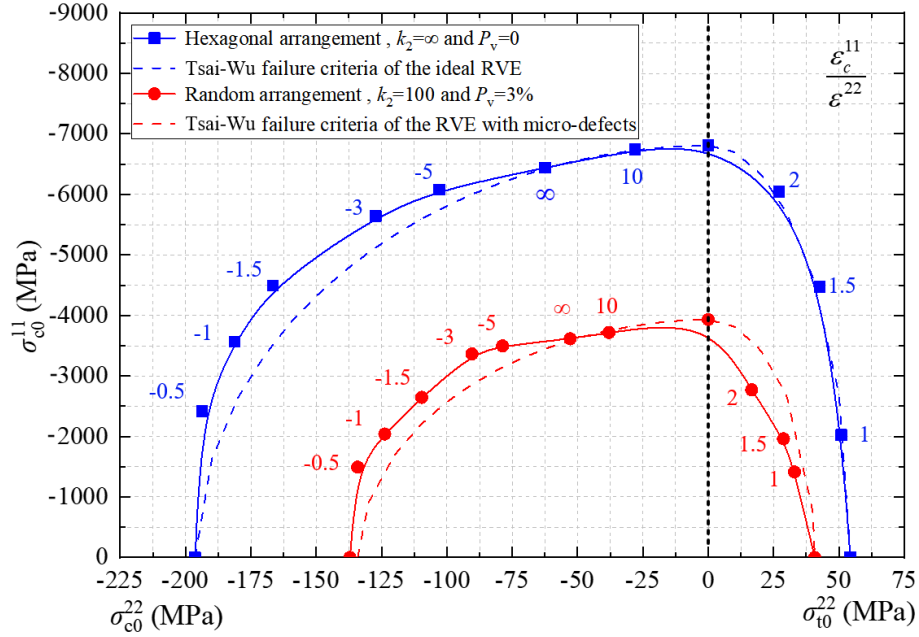


Fig. 24. The biaxial damage envelope of two configurations of RVEs

## 5. Conclusions

This study quantitatively assessed the effects of three micro-defects, i.e., geometric fiber arrangement, fiber misalignment, and micro-voids, on the strength and failure mechanism of UD-FRP using a computational micromechanics framework. These micro-defects were implemented with self-defined parameter regulation, where the method to characterize fiber misalignment based on random walk algorithm has been optimized to quickly generate periodic RVE of UD-FRP. The individual and interactive effect of micro-defects on the mechanical performance was analyzed. The part of individual effects is in good agreement with the results of previous research. At the same time, the results also supplement parts not mentioned in previous research, such as the influence of fiber arrangement on longitudinal shear strength. Meanwhile, the detailed analysis was conducted on the interactions and internal mechanisms between micro-defects. The analysis results of this paper can provide reference for defects control in the FRP manufacturing process. Micro-voids can be controlled by degassing and the flow process in infusion or intelligently adjusting the curing parameters during the autoclave process. Fiber arrangement and fiber misalignment can be controlled in the lay-up when prepregs are made or the fibers are produced etc. The main conclusion includes the following aspects.

(1) Detailed analysis was conducted on the individual effects of three micro-defects on the mechanical properties of UD-FRP under various load forms, supplementing some of the effects not previously investigated in previous studies. The longitudinal compressive strength of UD-FRP is adversely affected by all three types of micro-defects. Fiber misalignment has the most significant impact and also causes a reduction in the longitudinal stiffness of UD-FRP. However, it does not significantly affect the transverse properties. Conversely, the transverse tensile and compressive strength of UD-FRP is significantly reduced by the presence of micro-voids and the random arrangement of fibers. Micro-voids reduce the strength of transverse and longitudinal shear, and it is worth noting that the fiber arrangement also has a significant impact on longitudinal shear. The

---

modulus of transverse tension and compression is influenced by micro-voids, but this effect is not observed under shear load. Finally, quantify and summarize the impact of micro-defects with different parameters under different load forms, providing reference to control the most influencing defects in the manufacturing of FRP.

(2) Obvious interactions were examined between the micro-defects under longitudinal compression. The weakening effect of random fiber arrangement on longitudinal compressive strength is exacerbated by local fiber micro-buckling due to fiber misalignment. However, the presence of micro-voids actually reduces this weakening effect by introducing new stress concentrations in RVEs with a hexagonal arrangement. It is important to note that there is no direct interaction between fiber misalignment and micro-voids. Meanwhile, there is no noticeable interaction between the three micro-defects under transverse tension/compression and transverse shear, but as for longitudinal shear, the increase in micro-voids contents significantly reduces the strength difference caused by the fiber arrangement.

(3) The combined loading of longitudinal compression and transverse tension/compression under different ratios were applied respectively to investigate the biaxial damage envelope for the ideal RVE (hexagonal fiber arrangement, straight fibers, and no micro-voids) and the RVE with all three kinds of micro-defects (random fiber arrangement, high fiber misalignment  $k_2=100$ , and high porosity  $P_v=3.0\%$ ). For the failure strength under the combined longitudinal compression and transverse tension, the theoretical predictions are in good agreement with the results obtained from numerical simulations. However, the computational micromechanics-predicted strengths for both two configurations of RVE are slightly higher than the Tsa-Wu criteria for combined longitudinal and transverse compression.

The ultimate mechanical properties of unidirectional fiber-reinforced polymers UD-FRP are subject to the combined influence of multiple micro-defects discussed in this article, resulting in substantial variations in the mechanical characteristics. The research conducted in this study serves as an essential foundation for quantifying this inherent uncertainty. The future research work in this area should focus on establishing an uncertainty analysis framework, which will encompass considerations of micro-defects and interlayer delamination, with the aim of precisely forecasting variations in the mechanical properties of laminates. Additionally, relevant experiments will be designed to validate the uncertainty analytical system, as well as the results presented within this article. The results will be reported when the work is completed.

## References

- [1] M. Chiachio, J. Chiachio, G. Rus, Reliability in composites – A selective review and survey of current development, *Composites Part B* 43(3) (2012) 902-913.
- [2] S. Zhang, C. Zhang, X. Chen, Effect of statistical correlation between ply mechanical properties on reliability of fibre reinforced plastic composite structures, *Journal of Composite Materials* (2014).
- [3] X.Y. Zhou, S.Y. Qian, N.W. Wang, W. Xiong, W.Q. Wu, A review on stochastic multiscale analysis for FRP composite structures, *Composite structures* (Mar.) (2022) 284.
- [4] A. Sharma, S. Daggumati, A. Gupta, W. Van Paepegem, On the prediction of the bi-axial failure envelope of a UD CFRP composite lamina using computational micromechanics: Effect of microscale parameters on macroscale stress-strain behavior, *Composite Structures* 251 (2020).
- [5] J.C. Garcia-Merino, C. Calvo-Jurado, E. Garcia-Macias, Polynomial chaos expansion for uncertainty propagation analysis in numerical homogenization of 2D/3D periodic composite microstructures, *Composite Structures* 300 (2022).
- [6] M. Tootkaboni, L. Graham-Brady, A multi-scale spectral stochastic method for

---

homogenization of multi-phase periodic composites with random material properties, *International Journal for Numerical Methods in Engineering* 83(1) (2010) 59-90.

[7] J. Zhi, T.-E. Tay, Computational structural analysis of composites with spectral-based stochastic multi-scale method, *Multiscale and Multidisciplinary Modeling Experiments and Design* 1(2) (2018) 103-118.

[8] M. Mehdikhani, I. Straumit, L. Gorbatiikh, S.V. Lomov, Detailed characterization of voids in multidirectional carbon fiber/epoxy composite laminates using X-ray micro-computed tomography, *Composites Part a-Applied Science and Manufacturing* 125 (2019).

[9] M. Poulton, W. Sebastian, Taxonomy of fibre mat misalignments in pultruded GFRP bridge decks, *Composites Part a-Applied Science and Manufacturing* 142 (2021).

[10] X. Wang, Z. Guan, S. Du, G. Han, M. Zhang, A long-range force based random method for generating anisotropic 2D fiber arrangement statistically equivalent to real composites, *Composites Science and Technology* 180 (2019) 33-43.

[11] M. Hojo, M. Mizuno, T. Hobbiebrunken, T. Adachi, M. Tanaka, S.K. Ha, Effect of fiber array irregularities on microscopic interfacial normal stress states of transversely loaded UD-CFRP from viewpoint of failure initiation, *Composites Science and Technology* 69(11-12) (2009) 1726-1734.

[12] M. Marco, E. Giner, M.H. Miguelez, D. Gonzalez, On the effect of geometrical fiber arrangement on damage initiation in CFRPs under transverse tension and compression, *Composite Structures* 274 (2021).

[13] F.C. Huang, X.F. Pang, F.L. Zhu, S.F. Zhang, Z.W. Fan, X. Chen, Transverse mechanical properties of unidirectional FRP including resin-rich areas, *Computational Materials Science* 198 (2021).

[14] A. Wongsto, S. Li, Micromechanical FE analysis of UD fibre-reinforced composites with fibres distributed at random over the transverse cross-section, *Composites Part a-Applied Science and Manufacturing* 36(9) (2005) 1246-1266.

[15] T.J. Vaughan, C.T. McCarthy, A micromechanical study on the effect of intra-ply properties on transverse shear fracture in fibre reinforced composites, *Composites Part a-Applied Science and Manufacturing* 42(9) (2011) 1217-1228.

[16] B.N. Fedulov, F.K. Antonov, A.A. Safonov, A.E. Ushakov, S.V. Lomov, Influence of fibre misalignment and voids on composite laminate strength, *Journal of Composite Materials* 49(23) (2015) 2887-2896.

[17] T.A. Sebaey, G. Catalanotti, C.S. Lopes, N. O'Dowd, Computational micromechanics of the effect of fibre misalignment on the longitudinal compression and shear properties of UD fibre-reinforced plastics, *Composite Structures* 248 (2020).

[18] L.F. Varandas, G. Catalanotti, A.R. Melro, R.P. Tavares, B.G. Falzon, Micromechanical modelling of the longitudinal compressive and tensile failure of unidirectional composites: The effect of fibre misalignment introduced via a stochastic process, *International Journal of Solids and Structures* 203 (2020) 157-176.

[19] L. Zhang, S.F. Zhang, D. Xu, X. Chen, Compressive behavior of unidirectional FRP with spacial fibre waviness and non-uniform fibre packing, *Composite Structures* 224 (2019).

[20] A. Hyde, J.L. He, X.D. Cui, J. Lua, L. Liu, Effects of microvoids on strength of unidirectional fiber-reinforced composite materials, *Composites Part B-Engineering* 187 (2020).

[21] D.A. Vajari, C. Gonzalez, J. Llorca, B.N. Legarth, A numerical study of the influence of microvoids in the transverse mechanical response of unidirectional composites, *Composites Science and Technology* 97 (2014) 46-54.

[22] C.W. He, J.R. Ge, X.F. Cao, Y.F. Chen, H.S. Chen, D.N. Fang, The effects of fiber radius and fiber shape deviations and of matrix void content on the strengths and failure mechanisms of UD composites by computational micromechanics, *Composites Science and Technology* 218 (2022).



- 
- [23] Z.H. Tang, L.C. Guo, Z.X. Li, K. Huang, T. Zheng, R.J. Sun, A comparative study of void characteristics on the mechanical response of unidirectional composites, *Mechanics of Materials* 174 (2022).
- [24] M. Mehdikhani, L. Gorbatikh, I. Verpoest, S.V. Lomov, Voids in fiber-reinforced polymer composites: A review on their formation, characteristics, and effects on mechanical performance, *Journal of Composite Materials* 53(12) (2019) 1579-1669.
- [25] N. Kosmann, J.M. Karsten, M. Schuett, K. Schulte, B. Fiedler, Determining the effect of voids in GFRP on the damage behaviour under compression loading using acoustic emission, *Composites Part B-Engineering* 70 (2015) 184-188.
- [26] P.M. Moran, X.H. Liu, C.F. Shih, KINK BAND FORMATION AND BAND BROADENING IN FIBER COMPOSITES UNDER COMPRESSIVE LOADING, *Acta Metallurgica Et Materialia* 43(8) (1995) 2943-2958.
- [27] T. Zheng, L.C. Guo, R.J. Sun, Z.X. Li, H.J. Yu, Investigation on the compressive damage mechanisms of 3D woven composites considering stochastic fiber initial misalignment, *Composites Part a-Applied Science and Manufacturing* 143 (2021).
- [28] Y.J. Li, B. Stier, B. Bednarczyk, J.W. Simon, S. Reese, The effect of fiber misalignment on the homogenized properties of unidirectional fiber reinforced composites, *Mechanics of Materials* 92 (2016) 261-274.
- [29] C.J. Creighton, M.P.F. Sutcliffe, T.W. Clyne, A multiple field image analysis procedure for characterisation of fibre alignment in composites, *Composites Part a-Applied Science and Manufacturing* 32(2) (2001) 221-229.
- [30] W.J.R. Christian, F.A. DiazDelaO, K. Atherton, E.A. Patterson, An experimental study on the manufacture and characterization of in-plane fibre-waviness defects in composites, *Royal Society Open Science* 5(5) (2018).
- [31] S. Qi, O. Alajarmeh, T. Shelley, P. Schubel, K. Rendle-Short, X. Zeng, Fibre waviness characterisation and modelling by Filtered Canny Misalignment Analysis (FCMA), *Composite Structures* 307 (2023).
- [32] T.A. Sebaey, G. Catalanotti, N.P. O'Dowd, A microscale integrated approach to measure and model fibre misalignment in fibre-reinforced composites, *Composites Science and Technology* 183 (2019).
- [33] G. Catalanotti, T.A. Sebaey, An algorithm for the generation of three-dimensional statistically Representative Volume Elements of unidirectional fibre-reinforced plastics: Focusing on the fibres waviness, *Composite Structures* 227 (2019).
- [34] J.E. Little, X.W. Yuan, M.I. Jones, Characterisation of voids in fibre reinforced composite materials, *Ndt & E International* 46 (2012) 122-127.
- [35] G. Catalanotti, On the generation of RVE-based models of composites reinforced with long fibres or spherical particles, *Composite Structures* 138 (2016) 84-95.
- [36] L. Chapelle, M. Levesque, P. Brondsted, M.R. Foldschack, Y. Kusano, GENERATION OF NON-OVERLAPPING FIBER ARCHITECTURE, 20th International Conference on Composite Materials (ICCM), Copenhagen, DENMARK, 2015.
- [37] H. Altendorf, D. Jeulin, Random-walk-based stochastic modeling of three-dimensional fiber systems, *Physical Review E* 83(4) (2011).
- [38] M. Mehdikhani, N.A. Petrov, I. Straumit, A.R. Melro, S.V. Lomov, L. Gorbatikh, The effect of voids on matrix cracking in composite laminates as revealed by combined computations at the micro- and meso-scales, *Composites Part a-Applied Science and Manufacturing* 117 (2019) 180-192.
- [39] X.Y. Hui, Y.J. Xu, W.H. Zhang, An integrated modeling of the curing process and transverse tensile damage of unidirectional CFRP composites, *Composite Structures* 263 (2021).
- [40] A. Sharma, S. Daggumati, A. Gupta, W. Van Paepegem, On the prediction of the bi-axial



---

failure envelope of a UD CFRP composite lamina using computational micromechanics: Effect of microscale parameters on macroscale stress–strain behavior, *Composite Structures* 251 (2020).

[41] C. Gonzalez, J. Llorca, Mechanical behavior of unidirectional fiber-reinforced polymers under transverse compression: Microscopic mechanisms and modeling, *Composites Science and Technology* 67(13) (2007) 2795-2806.

[42] I.M. Gitman, H. Askes, L.J. Sluys, Representative volume: Existence and size determination, *Engineering Fracture Mechanics* 74(16) (2007) 2518-2534.

[43] M.I. Okereke, A.I. Akpoyomare, A virtual framework for prediction of full-field elastic response of unidirectional composites, *Computational Materials Science* 70 (2013) 82-99.

[44] D. Pulungan, G. Lubineau, A. Yudhanto, R. Yaldiz, W. Schijve, Identifying design parameters controlling damage behaviors of continuous fiber-reinforced thermoplastic composites using micromechanics as a virtual testing tool, *International Journal of Solids and Structures* 117 (2017) 177-190.

[45] N. Triantafyllidis, S. Bardenhagen, The influence of scale size on the stability of periodic solids and the role of associated higher order gradient continuum models, *Journal of the Mechanics and Physics of Solids* 44(11) (1996) 1891-1928.

[46] R. Gutkin, S.T. Pinho, P. Robinson, P.T. Curtis, Micro-mechanical modelling of shear-driven fibre compressive failure and of fibre kinking for failure envelope generation in CFRP laminates, *Composites Science and Technology* 70(8) (2010) 1214-1222.